8-6-2009

A Hybrid Method for Predicting Lift and Drag of Semi-planing/ Semi-displacement Hull Forms

Brandon Taravella
University of New Orleans

A Hybrid Method for Predicting Lift and Drag of Semi-planing/Semi-displacement Hull Forms

A Dissertation

Submitted to the Graduate Faculty of the
University of New Orleans
in partial fulfillment of the
requirements for the degree of

Doctor of Philosophy
in
Engineering and Applied Science
Naval Architecture and Marine Engineering

by

Brandon M. Taravella

B.S. University of New Orleans, 2003
M.S. University of New Orleans, 2005

August, 2009

DEDICATION

To my wife, Shana, for all of her love and support.

Acknowledgement

I am very grateful to Dr. William S. Vorus, my dissertation advisor. His continuous guidance, encouragement and support made it possible for me to complete this dissertation.

I would also like to thank Dr. Lothar Birk, Dr. Kazim Akyuzlu, Dr. Martin Guillot, Dr. J. Alex McCorquodale and Dr. Dongming Wei for serving on my dissertation committee and providing additional technical guidance.

Dr. Russell Trahan and Dr. Norman Whitley should also be thanked for their continuous encouragement throughout my studies at the University of New Orleans.

The Office of Naval Research Modeling and Optimization Program should be mentioned for providing funding (2003-2006).

Last but not least, I would like to thank my family and friends, especially my wife Shana, for their support, encouragement and understanding throughout the years that I have been completing my doctoral work.

Table of Contents

List of Figures and Tables

Abstract

With the ever present desire for ships and boats to run faster while carrying a greater load, a need exists to reduce the drag while simultaneously increasing hydrodynamic lift. Therefore, a need for semi-planing/semi-displacement hullforms exists for vessels to carry relatively high loads (between 500 and 3000 tons) with a general length Froude number range between 0.4 and 1.0.

A hybrid method for calculating the lift and drag of semi-planing/semi-displacement hull forms is developed. This is done by separating the kinematic boundary condition into odd and even parts. The odd and even parts of the kinematic boundary condition are solved independently along with the free-surface boundary condition and superimposed for a complete "hybrid" solution.

The superimposed solution components relate to Michell's (1898) "thin ship" integral for odd flow and Maruo's (1967) "flat ship" integral for even flow. A generalized form of Michell's (1898) integral is provided for high speed slender bodies by implementing a more realistic near field condition (Ogilvie, 1975) and a wake trench (Vorus, 2009). A generalized form of Maruo's (1967) integral has also been developed. Comparisons of the generalized methods have been made with available model test and/or analytical data.

With this, the concept of the Semihull (Vorus, 2005) is revisited. Some results are given concerning the validity of the Semihull as compared to a traditional displacement ship. Hull form optimization is also explored and the deadrise angle distribution proves to be a major factor in calm water hydrodynamic performance.

Keywords: hydrodynamics, semi-planing, semi-displacement, Semihull

Introduction

With the ever present desire for ships and boats to run faster while carrying a greater load, a need exists to reduce the drag while simultaneously increasing hydrodynamic lift. However, a fully planing vessel may not always be the answer. For one reason, getting a large ship or boat to plane generally requires an unrealistic amount of power. There are also limitations with regards to structural integrity and seakeeping.

Therefore, a need for semi-planing/semi-displacement hullforms exists for vessels between 500 and 3000 tons. Particular interest has been placed, in recent years, on high-speed ferries, littoral combat ships, and high speed yachts. All are required to carry relatively high loads with a general length Froude number range between 0.4 and 1.0. (Lamb, 2003)

All surface ships or boats, regardless of size and/or hull form, develop some circulation induced lift, and associated drag. The lift can be either positive or negative and is affected by wave making. The wave drag is always positive. (Vorus, June 2005)

In typical "displacement" ship hulls, hydrodynamic lift is ignored. The Froude number is generally small enough (< 0.3), and the hulls symmetrical enough, that lift can be attributed purely to hydrostatics. The wave drag, which results from displacement effects only, is then considered. This wave drag can be predicted by various methods. One of which is the Michell-Kelvin thin ship theory (Michell, 1898) which has been widely studied and said to produce reasonably reliable, efficiently computed results. Michell's thin ship theory has also produced satisfactory results for shapes that would not be considered as "thin". (Tuck, 2002)

The purpose of this dissertation is to develop a hybrid method in which the hydrodynamic lift (including gravity effects) is calculated independently of hydrostatic lift and superimposed to

result in the total lift developed by the vessel. Investigations into wave drag and hull form optimization are also addressed.

Newman (1977) presents a linearized two-dimensional theory for flows past lifting foils. By linearizing the boundary conditions, Newman is able to separate the velocity potential into odd and even functions. The odd and even functions correspond to two different physical problems. The even function represents the effects of foil thickness while the odd function represents the effects of the surface's camber and angle of attack. Newman goes on to present the linear solution in which the thickness and lifting problems can be separated and solved independently. He does this by using a source distribution for the thickness and a vortex distribution for the lift. The two distributions are then superimposed to arrive at a complete solution.

Vorus (June 2005) proposed the idea of a thin-ship/flat-ship theory for the prediction of lift and wave resistance on semi-planing/semi-displacement hull forms. In his report, Vorus showed that the kinematic boundary condition could be separated into odd and even parts. The odd boundary condition, which corresponds to the transverse flow, can be used to predict the wave making resistance due to displacement. The even boundary condition, which corresponds to the vertical flow, can be used to predict the dynamic lift and wave making resistance due to circulation. It is this realization that allows one to separate the problem into an odd problem, which Vorus solved with Michell's thin ship theory (Michell, 1898), and into an even problem, which Vorus solved using Maruo's flat ship theory (Maruo, 1967 and Vorus, April 2005). In his work, Vorus presents some preliminary results and makes a comparison between a Hybrid Semihull and a Doubly Parabolic hull form. As this work is just an initial report, Vorus (June

2005) still leaves room for further development of the theory and also provides opportunity to determine an optimum design.

Faltinsen and Sun (2007) investigated the significance of gravity on planing vessel hydrodynamics by developing a "2D+t" theory. Of particular interest to Faltinsen and Sun was the jet flow and bow spray created where the hull surface interacts with the free surface. They used previously developed schemes to model the jet flow and cut-off the bow spray in order to avoid numerical errors due to small contact angle in water re-entry, respectively. Faltinsen and Sun's method yielded fairly good results for a prismatic hull in terms of generated lift and free surface profile form when compared to experimental data of both Savitsky (1964) and Troesch (1992). However, Faltinsen and Sun (2007) admit to having trouble capturing the 3-D effects on pressure near the transom stern. Faltinsen and Sun (2007) justify this inadequacy by concluding that there is an infinite pressure gradient at the transom which causes the pressure to rapidly decrease to atmospheric pressure. However, Faltinsen and Sun (2007) developed a semi-empirical correction to account for this shortcoming. In the end, Faltinsen and Sun (2007) draw three important conclusions to their analysis:

1.) Gravity effect is negligible forward of the chine wetting position, but it is more important when approaching the transom stern.
2.) Gravity is more important in the case of moderate planing (i.e. "hump" region or semi-planing/semi-displacement hulls).
3.) Gravity influences the hydrodynamic part of the force because it changes the fluid flow around the hull and affects the free surface elevation.

Maruo (1967) presents solutions for "flattish" ships, typical of planing hulls. In particular, he analyzes both the high-aspect ratio (i.e. beam >> length >> draft) and low-aspect

ratio (i.e. length >> beam >> draft) cases. Of particular interest here is the low-aspect ratio case, that is, slender ships. Maruo goes on to solve the Laplace equation using the linear free surface condition with the fluid velocity normal to the body surface being zero. In his formulation, Maruo develops an integral equation describing the flow around a planing surface. The kernel of Maruo's integral is highly singular which Maruo admits is a "formidable" task to solve generally. He goes on to make the assumption of very large Froude number and presents an explicit solution for a triangular hull surface with no twist (i.e. flat delta hydrofoil). Maruo's final results for the low-aspect ratio flat ship case indicate that the effect of gravity increases the planing lift.

Tuck (1975) also studied the low-aspect-ratio flat-ship integral equation of Maruo (1967). Tuck attempted to overcome the difficulty of Maruo's singularity by rewriting the equation in terms of the stream function. Tuck goes on to present the results of three waterplanes: blunt, delta, cusped. The "delta" waterplane is of direct comparison to Maruo's results. Tuck was able to mimic Maruo's results using his own formulation for large Froude numbers (i.e. $\nu < 1$). However, Tuck's results do not follow a straight line as Maruo's results do. Rather, Maruo's curve provides the asymptote for Tuck's results. Tuck goes on to mention that he does not seem very convinced of the accuracy his results. This is mainly due to the fact that his formulation is predicting negative loadings at certain areas of the "hull" while at lower Froude numbers. Tuck also encounters a singularity along the flat keel, which is not physical. Because Tuck's program is so "crude", he goes on to explain that he cannot determine if the physically unacceptable results are due to a breakdown in the theory or numerical errors.

Cole (1988) provides a solution to Maruo's low-aspect ratio case with an analytical example. She admits to initially attempting to solve the integral equation for the general case,

but came up short of a solution. However, the results of Cole's analytical solution do not go without merit. In this solution she discovers that the wave drag is the sum of the spray drag and the energy carried away by the vertical flow and free-surface waves.

Michell (1897) presents a general solution, in the form of an integral, to the wave resistance of a "thin" ship moving with uniform velocity in an inviscid liquid. Michell's Integral has been well known for over a century in the field of theoretical naval architecture. However, it has been only relatively recent that this method, in computational form, has been applied in the practical design of actual ships. Essentially, the only approximation is that the vessel is represented by a centerplane distribution of Havelock sources of strength proportional to the hull slope. Michell's Integral provides usefully reliable results. The only limitation is that the beam is small compared to the length; however, draft is irrelevant.

Vorus and Taravella (2008) suggest that Michell's Integral may be insufficient for high speed ships. There are two complications here: with transom sterns the integrated source strength does not close, and it must to satisfy continuity; and secondly, the standard Michell's Integral implies effectively a rigid-wall boundary condition on the near field free-surface .

In the first of these, the source strength deficit is physically in the wake trough in the free-surface aft of the transom. The effect of the wake trough is said to increase the effective length of the vessel, thus lowering its wave making resistance. Approximate modeling is employed here by extending the centerplane source panels downstream into the wake. Vorus (March 2009) developed a method for determining the "wake trench" downstream of high-speed vessels with blunt transom sterns. As with much of the other work cited here, the assumption of ideal irrotational flow is made and higher order terms are omitted to establish the linear dynamic boundary condition. Point sources are defined on the center plane of the wake trench. The

strengths of sources just aft of the transom are assumed to equal the strength of the sources just forward of the transom which can be determined from the Michell thin ship analysis (1898). A spatial step downstream is then presented for determining the remaining source strengths which then lead to the length of the trench. Vorus proceeds by making comparisons to published experimental data in which the length of the wake trench nicely compares. The length of the wake trench is important in a wave making resistance analysis because it increases the effective length of the vessel, thus decreasing the effective Froude number.

The second misrepresentation in the Michell's near field free-surface boundary condition is eliminated by reformulating the near field in terms of "slender body" theory, versus "thin body theory." This was originally completed by Ogilvie (1972). However, Ogilvie limited his results to wedge shaped bodies. Vorus and Taravella (2008) have developed a general solution based on Ogilvie's (1972) formulation which yields very accurate results for length Froude numbers greater than 0.38.

1.0 Presentation of Problem

1.1 Kinematic Boundary Condition

Consider a general floating body whose cross-section at an axial position x (downstream) is depicted in Figure 1.1.

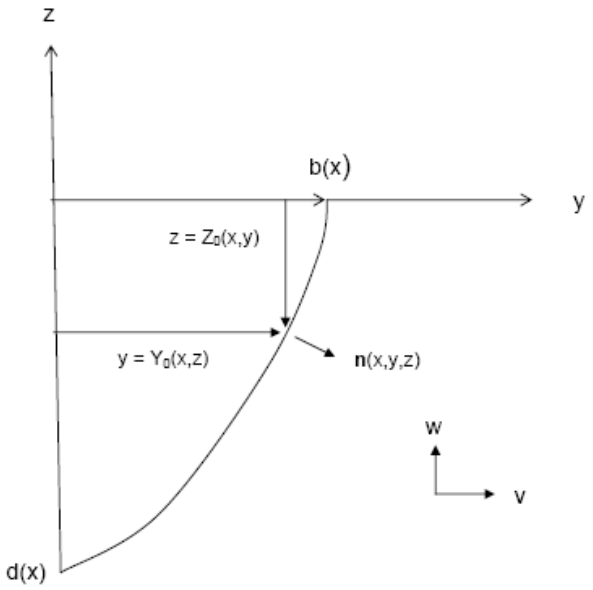

Figure 1.1 – Floating body cross section

The geometry of the floating body can be defined by either of the two surface functions:

$$F_y \equiv \pm y \mp Y_0(x,z) \tag{1.1}$$

or

$$F_z \equiv z - Z_0(x,y) \tag{1.2}$$

The plus/minus signs in equation (1.1) imply that a transversely symmetric hull is assumed so that Y_0 is an odd function with respect to $y = 0$.

The unit normal vector can be written for either equation (1.1) or (1.2) as

$$\vec{n} = \frac{\vec{\nabla} F}{\left|\vec{\nabla} F\right|} \tag{1.3}$$

for F either F_y or F_z.

The kinematic boundary condition on the body surface in the coordinate system translating with vessel speed U is:

$$\vec{V} \cdot \vec{n} = 0 \qquad \text{on } F = 0 \tag{1.4}$$

with

$$\vec{V} = (U + u)\vec{i} + v\vec{j} + w\vec{k} \tag{1.5}$$

Equations (1.4) and (1.5) along with (1.1) and (1.2) can be combined such that two alternative, but equivalent, kinematic boundary conditions exist.

From equations (1.1) and (1.5), we obtain

$$\pm v(x, Y_0, z) \mp (U + u) Y_{0x} \mp w Y_{0z} = 0 \quad \text{on } F_y = 0 \tag{1.6}$$

From equations (1.2) and (1.5), we obtain

$$w - (U + u) Z_{0x} \mp v Z_{0y} = 0 \qquad \text{on } F_z = 0 \tag{1.7}$$

Since both (1.6) and (1.7) equal zero, they are equal to each other and can be superimposed to produce yet a third form of the kinematic boundary condition:

$$\pm v(x,Y_0,z) \mp [U + u(x,Y_0,z)]Y_{0x} \mp w(x,Y_0,z)Y_{0z}$$

$$+ w(x,y,Z_0) - [U + u(x,y,Z_0)]Z_{0x} \mp v(x,y,Z_0)Z_{0y} = 0 \tag{1.8}$$

where, from Figure 1.1: $0 \le x \le l\,, 0 \le y \le b(x)\,, -d(x) \le z \le 0$ (1.9)

Provided the sum of the terms in equation (1.8) is collectively zero for all *x*, *y*, and *z* specified by (1.9), the kinematic condition of zero normal flow on the body surface is achieved. Note that equation (1.8) is a linear sum of terms that are either odd or even in *y* about the vertical centerplane. Equation (1.8) can therefore be re-separated into groups of even and odd terms, with both groups equal to zero.

$$\pm v(x,Y_0,z) \mp [U + u(x,Y_0,z)]Y_{0x} \mp w(x,Y_0,z)Y_{0z} \mp v(x,y,Z_0)Z_{0y} = 0 \tag{1.10}$$

$$w(x,y,Z_0) - [U + u(x,y,Z_0)]Z_{0x} = 0 \tag{1.11}$$

Now, neither equation (1.10) nor (1.11) correspond to zero normal flow on the body boundary, but their sum, equation (1.8), does.

The evenness and oddness of the groups of terms constituting equations (1.10) and (1.11) is now exploited in producing approximate solutions in the same general way as the superposition used with linearized hydrofoil theory (Newman, 1977). Recall that the section thickness offset is an odd function with respect to the meanline and the meanline camber is even. This characteristic reduces the solution to a superposition of independent solutions for a symmetric thickness form, producing an odd transverse flow with no lift, is in terms of sources, and the even camberline flow, which produces lift, is in terms of vortices. (Vorus, June 2005)

In order to produce a similar superimposed flow solution for the ship hull case, it is first necessary to linearize equations (1.10) and (1.11). We do this by assuming the velocity unknowns, as well as the geometry offsets and derivatives in (1.10) and (1.11) are small. Discarding the products and satisfying the resulting conditions on Y_0 and $Z_0 = 0$, respectively, gives:

$$\pm v(x,0,z) \mp UY_{0x}(x,z) = 0 \tag{1.12}$$

$$w(x,y,0) - UZ_{0x}(x,y) = 0 \tag{1.13}$$

Equations (1.12) and (1.13) are the standard linearized kinematic boundary conditions for two well known approximate solutions: the odd condition, equation (1.12), corresponds to a sheet of sources, $q(x,z)$, on the vertical hull centerplane, and the even condition, equation (1.13), corresponds to a sheet of transverse (or axial) vortices, $\gamma(x,y)$, on the undisturbed waterplane. The sources produce a transverse displacement flow without circulation and lift, and the vortices produce a purely lifting flow with circulation.

The first order free-surface boundary condition, similarly linearized, accompanies both equations (1.12) and (1.13).

$$gw(x,y,0) + U^2 u_x(x,y,0) = 0 \tag{1.14}$$

where g is the gravitational constant.

Adding a condition of no waves propagated upstream, equations (1.12) and (1.14) generate "Michell's Integral" (Michell, 1898), (Tuck, 1987) for thin ship wave resistance, and

equations (1.13) and (1.14) correspond to Maruo's "flat ship" theory for planing (Maruo, 1967), (Vorus, 2005), (Vorus and Taravella, 2009).

1.2 Solution Coupling

The solutions to these two ideal flow boundary-value problems are to be superimposed according to the separation at equation (1.8). The model is therefore that of a slender ship which is both thin, equation (1.12), and also flat, equation (1.13). The schematic model "T" cross-section is depicted on Figure 1.2.

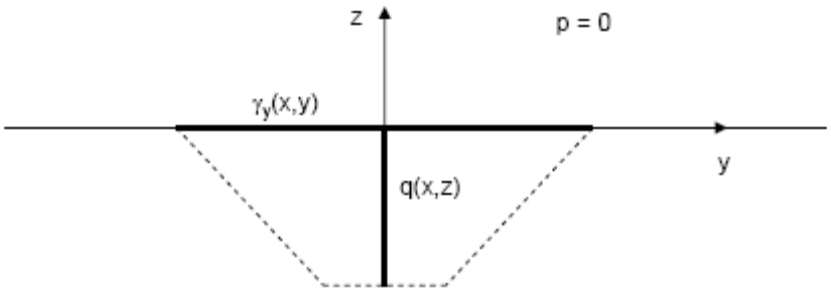

Figure 1.2 – Thin/Flat slender ship model (Sources and Vortices)

Coupling of the thickness, $q(x,z)$, and lifting, $\gamma(x,y)$, elements of this composite model must be addressed. The transverse vortices produce no transverse normal velocities, v, on the centerplane, so that q can be determined independently of γ_y. However, in general, the sources do produce a vertical normal velocity component on the waterplane.

2.0 Odd Flow

The wave resistance due to the odd flow can be addressed by using a form of the once forgotten "Michell's Integral" (Michell, 1898). Michell's integral provides a solution for the wave resistance of a thin-body (i.e. small beam).

Michell's integral along with equations (1.12) and (1.14) is straight forward. The standard models consist of a centerplane of source panels as depicted in Figure 2.1. The gradients in z are considered small relative to those in x and y, with the result (dimensionless on U):

$$q(x;z) = 2v(x,0;z) = 2h_x(x;z) \tag{2.1}$$

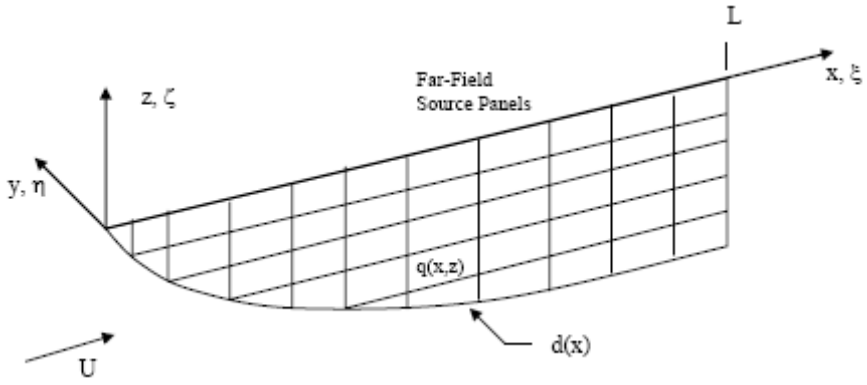

Figure 2.1 –Source Panel Arrangement for Michell's Integral Computation (no wake shown)

Michell's integral for wave resistance is formulated as:

$$D_w = \frac{\rho U^2 \kappa^2}{\pi} \int_{\lambda=1}^{\infty} \frac{\lambda^2}{\sqrt{\lambda^2 - 1}} \left(P^2 + Q^2\right) d\lambda \tag{2.2}$$

where D_w is the wave drag and κ is the wave number (i.e. $\kappa \equiv g/U^2$). P and Q are defined as:

$$P + iQ = \int_{x=0}^{L} \int_{z=0}^{d(x)} 2h_x e^{\kappa z \lambda^2} e^{i\kappa x \lambda} dx dz \tag{2.3}$$

The double integral of equation (2.3) can easily be executed analytically if one assumes that the source strength is constant on a given hull panel shown in Figure 2.1. Further, the integral of equation (2.2) can easily be computed numerically for general hull forms.

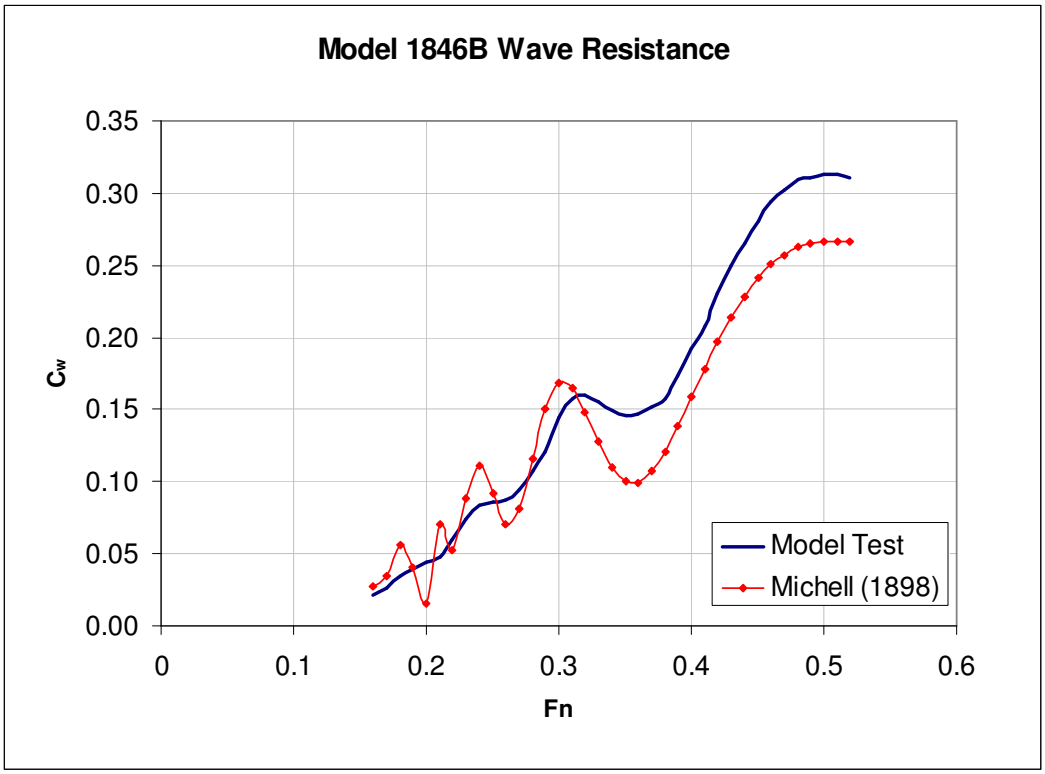

Figure 2.2 – Comparison of Wave Resistance for 1846B Model Test to Michell's (1898) Integral (Ogilvie, 1969)

Although Michell's integral (Michell, 1898) seems rather crude, the accuracy when compared to model tests, as in Figure 2.2, is not bad at low speeds ($Fn < 0.3$) and can provide similar results to most available CFD codes (which were not available to Michell) in a fraction of the computational time and effort. Since Michell's (1898) work, other authors including Tuck (1975); Tuck, Scullen and Lazauskas (2000) and (2002); and Vorus and Taravella (2008), to name a few, have expanded his work to address multi-hull vessels and high speed vessels. The work of Vorus and Taravella (2008) is presented herein.

2.1 Near Field Slender Body Theory

As can be seen from Figure 2.2, Michell's (1898) integral underestimates wave resistance at high speeds. While Michell's (1898) integral provides decent results for far field wave resistance, he does not address the influence of the near field flow. Although not explicitly stated by Michell (1898), further investigation by Vorus and Taravella (2008) led to the discovery that Michell's integral mimics the low speed free surface condition (transverse flow only-the free surface acts like a rigid wall) in the near field. The typical high speed free-surface condition (vertical flow only) was also investigated by Vorus and Taravella (2008), and it generated results that grossly overestimated model test results for wave resistance for the speed range of interest. (The latter results are presented in section 2.3 of this work.) It was therefore deemed necessary to develop a more accurate slender body method for the speed range of interest.

Ogilvie (1972) investigated a boundary element method for slender ships. In his method, Ogilvie recognized that near a slender ship's bow, rates of change of flow variables should be greater than those usually assumed by slender body theory. Ogilvie's result is still a slender body theory in that the rates of change in the near field are much greater in the transverse direction than in the longitudinal direction; however, the difference in order of magnitude between them is less than the usual slender body assumptions.

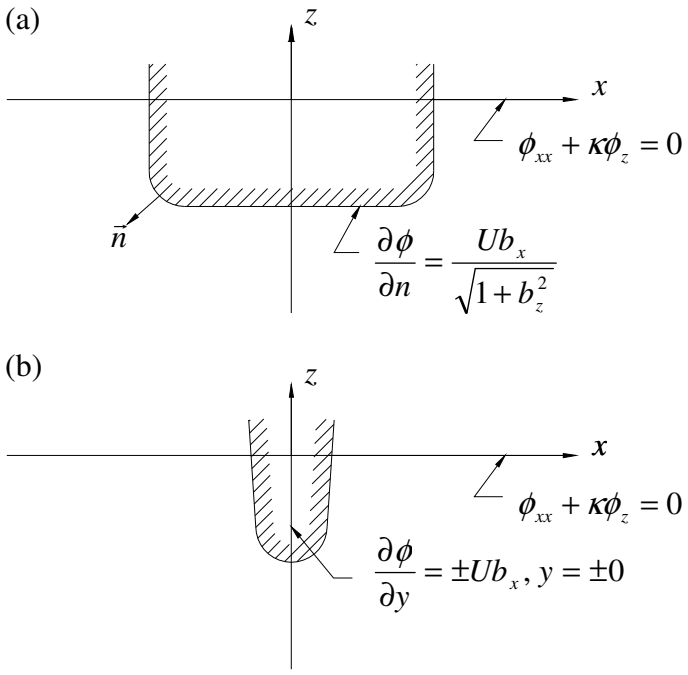

Figure 2.3 – Boundary conditions for the first approximation: (a) General body, (b) Thin body (Ogilvie, 1972)

From the thin body boundary conditions in Figure 2.3, an expression for the velocity potential was developed in Ogilvie (1972), equation 1 as:

$$\phi(x,y,z) = \mathrm{Re}\left\{+\frac{U}{\pi}\int_{-H(x)}^{0} b_x(x,\zeta)\ln(y+iz-i\zeta)d\zeta - \frac{U}{\pi}\int_{0}^{H(x)} b_x(x,-\zeta)\ln(y+iz-i\zeta)d\zeta\right.$$

$$\left. -\frac{1}{\pi i}\int_{-\infty}^{\infty}\frac{\psi(x,\eta)}{\eta-(y+iz)}d\eta\right\} \tag{2.4}$$

where the third integral is a velocity potential for any other source distribution which induces no net normal velocity component on $y = 0$ and $-H(x) < z < 0$. ψ is a linear auxiliary function.

2.1.1 Mathematical Formulation

The y and z components of velocity are found as:

$$\phi_y - i\phi_z = -\frac{U}{\pi}\int_{-H(x)}^{0}\frac{b_x(x,\zeta)}{i\zeta-(y+iz)}d\zeta + \frac{U}{\pi}\int_{0}^{H(x)}\frac{b_x(x,-\zeta)}{i\zeta-(y+iz)}d\zeta - \frac{1}{\pi i}\int_{-\infty}^{\infty}\frac{\psi_\eta(x,\eta)}{\eta-(y+iz)}d\eta \tag{2.5}$$

In order to satisfy the boundary condition on $y = \pm 0$, it is required that

$$\psi(x, y) = \psi(x, -y) \tag{2.6}$$

Ogilvie (1972) also found that by approaching the plane of the undisturbed free surface from below, we have

$$\lim_{z \uparrow 0} \{\phi(x, y, z)\} = \psi(x, z) \tag{2.7}$$

In equation (2.4), the first two integrals represent the flow due to a line of 2-D sources on the negative z axis and a line of sinks symmetrically located on the positive z axis. Alone, these two integrals result in the general high speed free-surface boundary condition—only vertical flow at the plane of the undisturbed free surface. The third integral, however, represents a flow with both vertical and horizontal components at the plane $z = 0$.

Substituting the above potential function into the free surface condition, we get:

$$\psi_{xx} - \frac{\kappa}{\pi} \int_{-\infty}^{\infty} \frac{\psi_\eta(x, \eta)}{\eta - y} d\eta = \frac{2U\kappa}{\pi} \int_{-H(x)}^{0} \frac{\zeta b_x(x, \zeta)}{\zeta^2 + y^2} d\zeta \tag{2.8}$$

The task at hand is to solve equation (2.8) for $\psi(x, \eta)$, then use the result in equation (2.4).

Ogilvie (1972) generated a solution for a particular hull form—wedge-like bodies. However, it is of interest of this work to utilize a general solution.

Vorus and Taravella (2008) developed a general solution to Ogilvie's (1972) formulation using the formulation in this section along with the integral formulation of Appendix A. The Fourier transformed equation for auxiliary function $\psi(x,y)$, from equation (2.8) is generalized as:

$$\psi^*_{xx}(x, \ell) + \kappa |\ell| \psi^*(x, \ell) = \frac{2U\kappa}{\pi} \int_{y=-\infty}^{\infty} \int_{\zeta=-H(x)}^{0} \frac{\zeta b_x(x, \zeta)}{\zeta^2 + y^2} d\zeta e^{-i\ell y} dy \tag{2.9}$$

We can solve the *y* integral of equation (2.9) by defining

$$I_y \equiv \int_{y=-\infty}^{\infty} \frac{e^{-i\ell y}}{\zeta^2 + y^2} dy = 2 \int_{y=0}^{\infty} \frac{e^{-i\ell y}}{\zeta^2 + y^2} dy \tag{2.10}$$

From integral formula 3.723.2 of Gradshteyn and Ryzhik (2000):

$$I_y = \frac{\pi}{2\zeta} e^{-|\ell||\zeta|} \tag{2.11}$$

Therefore, from equation (2.9):

$$\psi^*_{xx}(x,\ell) + \kappa|\ell|\psi^*(x,\ell) = -\frac{g}{U} \int_{\zeta=-H(x)}^{0} b_x(x,\zeta) e^{-|\ell||\zeta|} d\ell \tag{2.12}$$

We can now solve this ordinary differential equation and take the inverse transform.

The homogeneous solution of equation (2.12) becomes:

$$\psi^*_h(x,\ell) = C_1^* \cos\sqrt{\kappa|\ell|}x + C_2^* \sin\sqrt{\kappa\ell}x \tag{2.13}$$

Generate the particular solution by *Variation of Parameters* as in Hildebrand (1976):

$$\psi^*(x,\ell) = C_1^*(x) \cos\sqrt{\kappa|\ell|}x + C_2^*(x) \sin\sqrt{\kappa\ell}x \tag{2.14}$$

Define

$$u_1(x) = \cos\sqrt{\kappa|\ell|}x \tag{2.15}$$

$$u_2(x) = \sin\sqrt{\kappa\ell}x \tag{2.16}$$

Such that equation (2.14) becomes

$$\psi^*(x,\ell) = C_1^*(x)u_1(x) + C_2^*(x)u_2(x) \tag{2.17}$$

By taking the Wronskian, *W*,

$$W(u_1,u_2) = u_1 u_2' - u_1' u_2 = \sqrt{\kappa\ell} \tag{2.18}$$

we can generate the particular solution as:

$$\psi^*(x,\ell) = \int_x \frac{h(\xi)\left[u_1(\xi)u_2(x) - u_2(\xi)u_1(x)\right]}{W\left[u_1(\xi), u_2(\xi)\right]} d\xi + c_1 u_1(x) + c_2 u_2(x) \tag{2.19}$$

Where from equation (2.12):

$$h(x) = -\frac{g}{U} \int_{\zeta=H(x)}^{0} b_x(x,\zeta) e^{-|\ell||\zeta|} d\zeta \tag{2.20}$$

In equation (2.19), assume no wave ahead of the bow $x = 0$. This gives:

$$\psi^*(x,\ell) = \int_{\xi=0}^{x} \frac{h(\xi)\left[u_1(\xi)u_2(x) - u_2(\xi)u_1(x)\right]}{W\left[u_1(\xi), u_2(\xi)\right]} d\xi \tag{2.21}$$

Substitute equations (2.15), (2.16), (2.18) and (2.20) into equation (2.21):

$$\psi^*(x,\ell) = \sqrt{\frac{g}{|\ell|}} \int_{\xi=0}^{x} \int_{\zeta=-H(\xi)}^{0} b_x(\xi,\zeta) e^{-|\ell||\zeta|} \sin\left(\sqrt{\kappa|\ell|}(x-\xi)\right) d\zeta d\xi \tag{2.22}$$

The inverse transform is a cosine since the integrand is even in ℓ.

$$\psi(x,y) = \frac{\sqrt{g}}{\pi} \int_{\xi=0}^{x} \int_{\zeta=-H\zeta)}^{0} b_x(\xi,\zeta) \int_{\ell=0}^{\infty} \frac{e^{\zeta\ell}}{\sqrt{\ell}} \cos(\ell y) \sin\left(\sqrt{\kappa\ell}(x-\xi)\right) d\ell d\zeta d\xi \tag{2.23}$$

Make the change of variable $\ell = s^2$

$$\psi(x,y) = \frac{2\sqrt{g}}{\pi} \int_{\xi=0}^{x} \int_{\zeta=-H\zeta)}^{0} b_x(\xi,\zeta) \int_{s=0}^{\infty} e^{\zeta s^2} \cos(s^2 y) \sin\left(s\sqrt{\kappa}(x-\xi)\right) ds d\zeta d\xi \tag{2.24}$$

Using the integral formulation of Appendix A and making a change of variable from y to η, equation (2.24) becomes

$$\psi(x,\eta) = \frac{2\sqrt{g}}{\pi} \int_{\xi=0}^{x} \int_{\zeta=-H\zeta)}^{0} b_x(\xi,\zeta) I(x,\xi,\eta,\zeta) d\zeta d\xi \tag{2.25}$$

where $I(x,\xi,\eta,\zeta)$ can be determined from equation (A5).

For utilization in equation (2.5), it is necessary to take the derivative of equation (2.25) with respect to η.

$$\psi_\eta(x,\eta) = \frac{2\sqrt{g}}{\pi} \int_{\xi=0}^{x} \int_{\zeta=-H\zeta)}^{0} b_x(\xi,\zeta) \frac{dI(x,\xi,\eta,\zeta)}{d\eta} d\zeta d\xi \tag{2.26}$$

Here, $\frac{dI(x,\xi,\eta,\zeta)}{d\eta}$ can be determined from equation (A6) of Appendix A.

Thus, equation (2.5) becomes

$$\phi_y - i\phi_z = -\frac{U}{\pi} \int_{-H(x)}^{0} \frac{b_x(x,\zeta)}{i\zeta - (y+iz)} d\zeta + \frac{U}{\pi} \int_{0}^{H(x)} \frac{b_x(x,-\zeta)}{i\zeta - (y+iz)} d\zeta$$

$$-\frac{2\sqrt{g}}{\pi^2 i} \int_{\eta=-\infty}^{\infty} \int_{\xi=0}^{x} \int_{\zeta=-H\zeta)}^{0} \frac{b_x(\xi,\zeta)}{\eta - (y+iz)} \frac{dI(x,\xi,\eta,\zeta)}{d\eta} d\zeta d\xi d\eta \tag{2.27}$$

2.1.2 Numerical Analysis

Recall equation (2.5) and the body boundary condition,

$$\phi_y = \frac{b_x \sin\beta}{n_y} \tag{2.28}$$

$$\phi_z = \frac{b_x \sin\beta}{n_z} \tag{2.29}$$

and assume the source strengths on the right hand side as unknown, q, such that equation (2.27) becomes

$$\frac{b_x \sin\beta}{n_y} - i\frac{b_x \sin\beta}{n_z} = -\frac{U}{2\pi} \int_{-H(x)}^{0} \frac{q(x,\zeta)}{i\zeta - (y+iz)} d\zeta + \frac{U}{2\pi} \int_{0}^{H(x)} \frac{q(x,-\zeta)}{i\zeta - (y+iz)} d\zeta - I_\psi \tag{2.30}$$

where

$$I_\psi \equiv \frac{2\sqrt{g}}{\pi^2 i} \int_{\eta=-\infty}^{\infty} \int_{\xi=0}^{x} \int_{\zeta=-H\zeta)}^{0} \frac{b_x(\xi,\zeta)}{\eta - (y+iz)} \frac{dI(x,\xi,\eta,\zeta)}{d\eta} d\zeta d\xi d\eta \tag{2.31}$$

and $\frac{dI(x,\xi,\eta,\zeta)}{d\eta}$ can be determined from equation (A6) of Appendix A.

We can now change the limits of the second integral of equation (2.30) such that we are integrating over the wetted hull.

$$\frac{b_x \sin\beta}{n_y} - i\frac{b_x \sin\beta}{n_z} = -\frac{U}{2\pi}\int_{-H(x)}^{0} \frac{q(x,\zeta)}{i\zeta - (y+iz)}d\zeta - \frac{U}{2\pi}\int_{-H(x)}^{0} \frac{q(x,\zeta)}{-i\zeta - (y+iz)}d\zeta - I_\psi \tag{2.32}$$

Factoring, we have

$$\frac{b_x \sin\beta}{n_y} - i\frac{b_x \sin\beta}{n_z} = -\frac{U}{2\pi}\int_{-H(x)}^{0} q(x,\zeta)\left[\frac{1}{i\zeta - (y+iz)} - \frac{1}{i\zeta + (y+iz)}\right]d\zeta - I_\psi \tag{2.33}$$

We can now discretize the length of the hull (or hull and wake trench) by *Nx* and the draft at each *nx* by *Nz*. The discretization is as follows:

1) The z-axis is divided into *Nz* elements with $\Delta z = 1/Nz$
2) The $j = 1, Nz$ points (ζ-pts) at the element centers are the locations of the sources.
3) The $k = 1, Nz$ points (z-pts) at the element centers are *Nz* field points where the kinematic boundary condition is satisfied.

Following this discretization, equation (2.33) becomes:

$$\frac{b_{xnxj} \sin\beta_{nxj}}{n_{ynxj}} - i\frac{b_{xnxj} \sin\beta_{nxj}}{n_{znxj}} = -\frac{U}{2\pi}\sum_{k=1}^{Nz} q_{nxjk}\Delta\zeta_{nx}\left[\frac{1}{i\zeta_{nxk} - (y_{nxj} + iz_{nxj})} - \frac{1}{i\zeta_{nxk} + (y_{nxj} + iz_{nxj})}\right] - I_{\psi mx}$$

for $j = 1$ to Nz (2.34)

where

$$I_{\psi mx} \equiv \frac{2\sqrt{g}}{\pi^2 i}\sum_{-\infty}^{\infty}\sum_{i=1}^{nx}\sum_{k=1}^{Nz}\left[\frac{b_{xik}}{\eta - (y_{ik} + iz_{ik})}\frac{dI(x,\xi,\eta,\zeta)}{d\eta}\right]\Delta\zeta_i\Delta\xi\Delta\eta \tag{2.35}$$

Rearranging terms, we have

$$\frac{b_{xnxj}\sin\beta_{nxj}}{n_{ynxj}} - i\frac{b_{xnxj}\sin\beta_{nxj}}{n_{znxj}} = \frac{U}{2\pi}\sum_{k=1}^{Nz} q_{nxjk}\Delta\zeta_{nx}\left[\frac{1}{y_{nxj}+i(z_{nxj}+\zeta_{nxk})}+\frac{1}{y_{nxj}+i(z_{nxj}-\zeta_{nxk})}\right] - I_{\psi nx}$$

$$\text{for } j = 1 \text{ to } Nz \qquad (2.36)$$

Now, this set of linear equations can be solved for q_{nxjk} which is the near field source strength (for slender ships with a wake trench) which can be used in a modified version of Michell's Integral. Equation (2.36) should be executed along the x-axis starting at the bow, nx = 1, to the stern (or end of wake trench), $nx = Nx$. It is important to note that there is an upstream dependence in the $I_{\psi nx}$ term, equation (2.35). It is this upstream dependence that makes it necessary to resort to the modified Michell's Integral of section 2.3 for slender vessels with a wake trench.

While ships without a wake trench are not of interest for this work, it is worth mentioning that the generalized Ogilvie (1972) formulation of Vorus and Taravella (2008) can also be used to directly calculate the wave resistance for those vessels with closed sterns. Once the source strengths are determined from equation (2.36), the total velocity potential can be approximated by parallel flow superimposed by the residual flow from equation (2.4). The velocity field can then be determined, and Bernoulli's equation can then be used to calculate the hull surface pressure. Integration of the hull surface pressure over the hull surface will result in the wave resistance.

2.2 Wake Trench

Vorus (March 2009) developed a wake trench analysis that can be used directly with the modified Michell Integral of section 2.3.

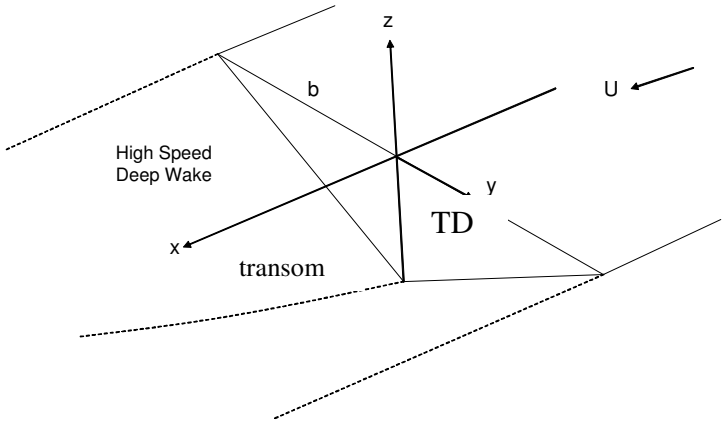

Figure 2.4 – Wake trench geometry

By using the typical assumption of ideal irrotational flow, a linear boundary condition and a sheet of sources on the centerplane of the wake trench, Vorus arrived at the following equation:

$$\frac{1}{2\pi}\int_{\xi=-1}^{0}\tilde{q}_i(\xi)\left(\frac{2\xi}{\zeta^2-\xi^2}-\frac{T_i}{T_{xi}}\frac{1}{\zeta\Delta x_i}\ln\frac{|\zeta-\xi|}{|\zeta+\xi|}\right)d\xi=\frac{1}{F_{nb}^2}\frac{T_i}{T_{xi}}-\frac{T_{i-1}}{T_{xi}}\frac{\tilde{\phi}_{i-1}(\zeta)}{\zeta\Delta x_i} \tag{2.37}$$

Equation (2.37) is discretized along the *x*-axis and solved in a spatial stepping manner. The length of the wake trench is when the trench depth at a given *x* position (T_{xi}) approaches zero.

The results of Vorus' analysis as presented in Figure 2.5 compare very well with those of experiments performed by Doctors and Beck (2005).

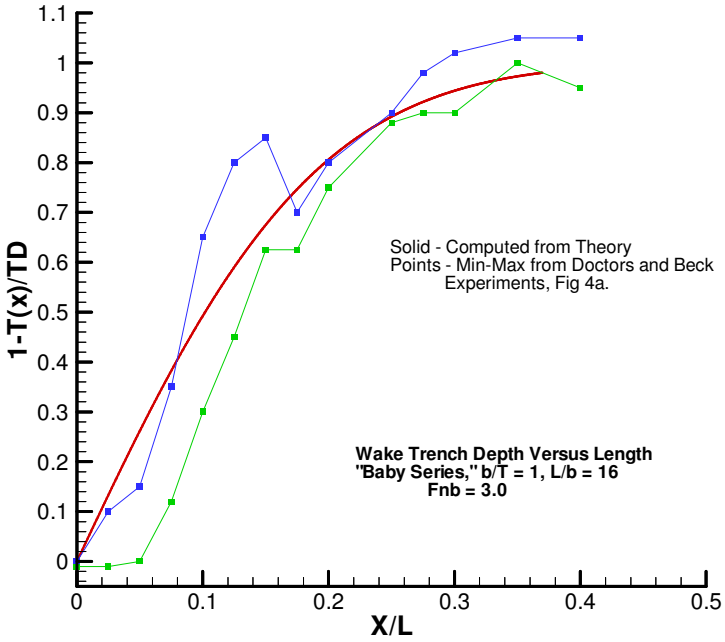

Figure 2.5 - Wake Trench Depth Versus Length for *Fnb* = 3.0, Calculations and Experimental Envelope (Vorus, March 2009)

2.3 High Speed Michell's Integral

After determining the strengths of the sources of the hull as outlined in section 2.1, these sources are collapsed to the centerplane. It is necessary to revert back to Michell's integral instead of using Ogilvie's (1972) formulation exclusively because of the wake trench. Since Ogilvie's formulation is a downstream stepping sequence, the downstream effects do not reflect upstream. Therefore, the effects of the wake trench are not properly ordered. The hull centerplane source strengths are used in conjunction with the centerplane source strength of the wake trench to determine the drag on the hull due to centerplane wave making sources.

The generalized Michell's integral thus becomes:

$$D_w = \frac{\rho U^2 \kappa^2}{\pi} \int_{\lambda=1}^{\infty} \frac{\lambda^2}{\sqrt{\lambda^2 - 1}} \left(PP_1 + QQ_1 \right) d\lambda \tag{2.38}$$

P, Q, P_1 and Q_1 are defined as:

$$P + iQ = \int_{x=0}^{L} \int_{z=0}^{d(x)} 2h_x e^{\kappa z \lambda^2} e^{i\kappa x \lambda} dx dz \tag{2.39}$$

$$P_1 + iQ_1 = \int_{x=0}^{L_w} \int_{z=0}^{d(x)} q(x,z) e^{\kappa z \lambda^2} e^{i\kappa x \lambda} dx dz \tag{2.40}$$

where L_w in equation (2.40) is the wake trench length discussed in section 2.2.

2.4 Results

The results for wave resistance using the high-speed formulation of sections 2.1 and 2.3 were calculated and compared to model test data for models 1846B and N43 as shown in Appendix B. The model test data was obtained from Ogilvie (1969). Since these models have closed sterns, as typical of most displacement hulls, the wake trench was not considered. The wake trench will be considered in later analysis for semi-planing/semi-displacment hull forms in which a transom stern does exist.

Both models used in the calculations, 1846B and N43, have a length of 16 ft, beam of 1.5 ft and a draft of 1 ft. A discretization of 20 x 20 was chosen and deemed to give very reliable results. It is noted that increasing the discretization significantly increases the calculation time. This has been attributed to the "infinite" summation of equation (2.36) required for each centerplane panel which has to be handled numerically in the code.

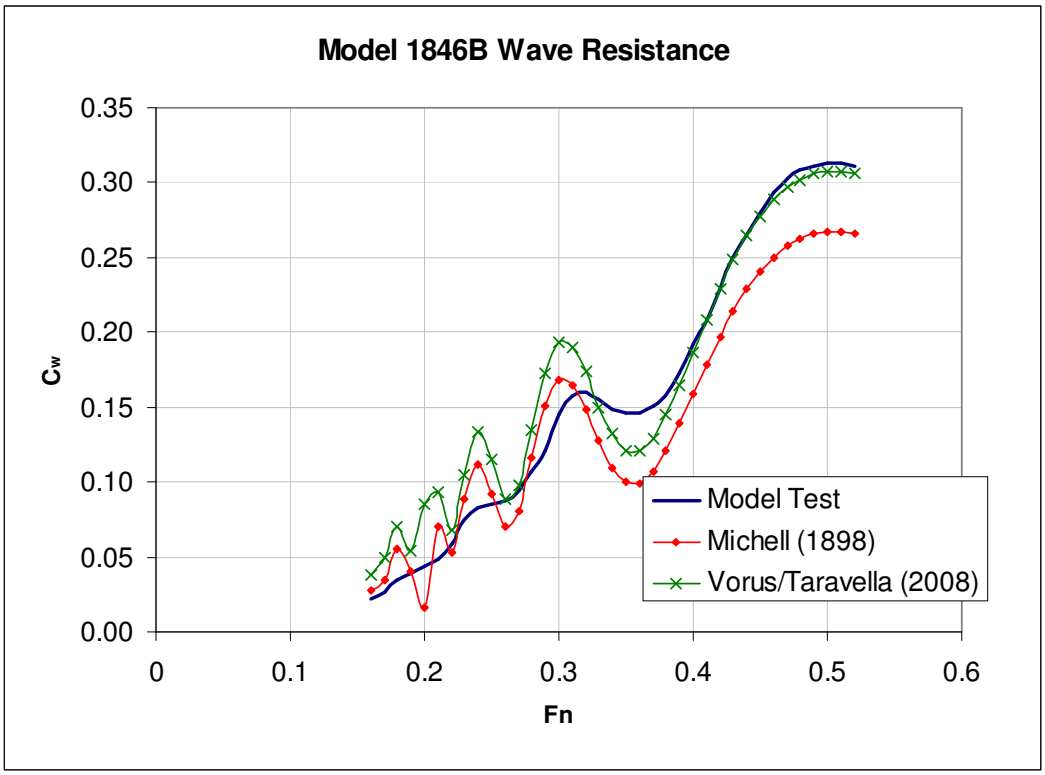

Figure 2.6 – Comparison of wave resistance calculations from Michell (1898) and Vorus/Taravella (2008) to model test data (Ogilvie, 1969) for Model 1846B

As can be seen from Figures 2.6 and 2.7, the method originally presented by Ogilvie (1972) and generalized by Vorus and Taravella (2008) yields excellent results for Froude numbers greater than 0.38 for these particular hull forms. This Froude number range and length-to-beam ratio used in the analysis above is directly applicable to the hull forms being studied in this work.

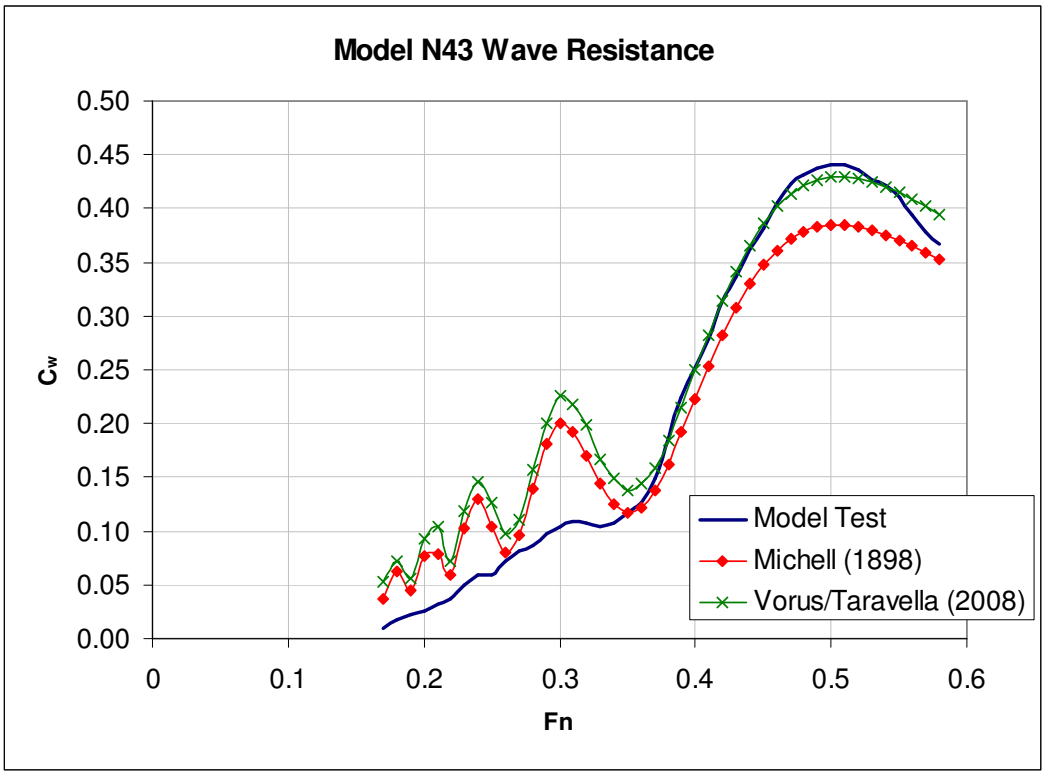

Figure 2.7 – Comparison of wave resistance calculations from Michell (1898) and Vorus/Taravella (2008) to model test data (Ogilvie, 1969) for Model N43

It is also noted that at low Froude numbers, the results of Vorus and Taravella (2008) seem to oscillate heavily. By comparison to the results of Michell's integral (1898), it is deemed that these oscillations are the result of the far-field wave formulation and not the formulation of the near field as presented in section 2.1. The influence of the near field formulation seems to slightly increase the results of Michell's integral.

In addition to the formulation of section 2.1 and 2.3 for determining the source strength, Vorus and Taravella (2008) also investigated the use of the typical high-speed near field free-surface condition which states that flow only exists in the vertical direction across the $z = 0$ plane. This was done in an effort to save computational time while still using the typical high speed free surface boundary condition, and it was accomplished by placing negative images of

the centerplane sources above the waterline. The results of this analysis, as shown in Figure 2.8, grossly over-estimated the wave making resistance and were deemed as not satisfactory for the speed range of interest.

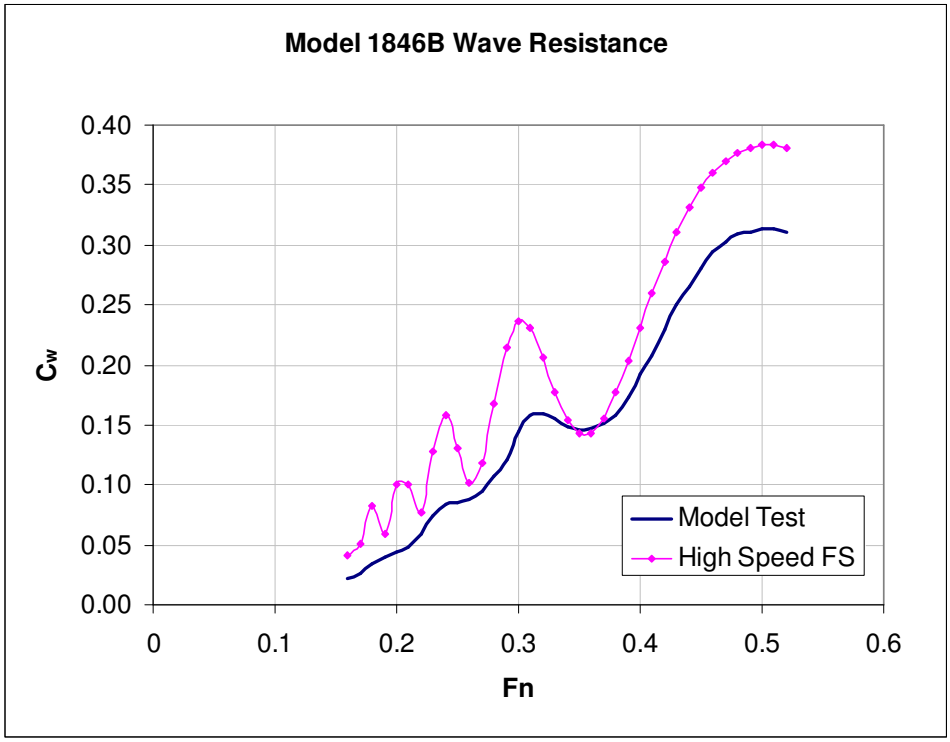

Figure 2.8 – Comparison of Wave Resistance for 1846B Model Test to Michell's (1898) Integral with High Speed Free-Surface Condition (Vorus/Taravella, 2008)

3.0 Even Flow

When the lift of a vessel exhibits significant dynamic lift (as is the case for full planing or semi-planing/semi-displacement hull forms) fluid sources alone are not applicable. Either vortices or doublets are needed to capture the circulation processes.

Maruo's (1967) integral is based on ideal flow theory and represents a solution to the Laplace equation for a velocity potential, subject to the linearized free surface boundary condition, with gravity included, and a radiation condition of no waves far upstream.

Referring to Figure 3.1, x is positive downstream with the coordinate system located at the bow and z is positive up. The planing surface is considered to occupy the region of the $z = 0$ plane corresponding to $-Y(x) \le y \le Y(x)$ and $0 \le x \le L$. The kinematic boundary condition is satisfied on the surface, $z = 0$. The Maruo theory can therefore be considered a "flat ship" theory (Tuck, 1975), in the same sense that Michell's integral is called "thin ship" theory.

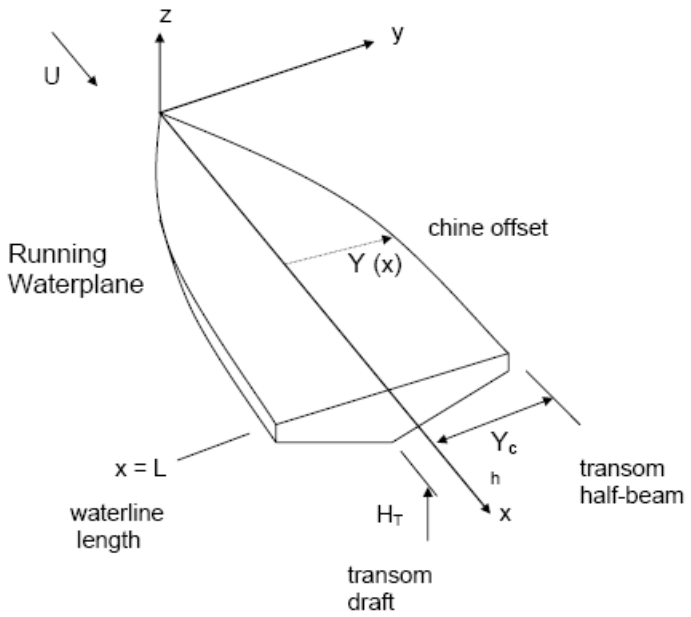

Figure 3.1 – Coordinate system and nomenclature for even flow problem

Maruo reduces his general formulation in the limits of high and low aspect ratio to "thin" and "slender" bodies, respectively. It is the slender body formulation of interest here due to its applicability to planing, or semi-planing, craft. The craft must therefore have wetted geometry that can be characterized as both "flat and slender."

3.1 Slender Body Theory and Formulation

The basis for slender body theory is that the gradients of both the body geometry and the flow variables are larger in cross sectional dimensions (y and z) than in x. For consistency of order of magnitudes of the terms retained in the linearized free-surface boundary condition, it is also required that the Froude number, *Fn*, be large on the order of the square-root of length-to-beam ratio. This leads to slender body equations that are parabolic in x and elliptic in the cross-sectional dimensions y and z.

The Maruo integral for slender planing surface is from Maruo (1967), equation 55:

$$\Phi(x,y,z) = -\frac{1}{\pi}\int_{\eta=-Y(x)}^{Y(x)}\int_{\xi=0}^{x}\gamma_y(\xi,\eta)\int_{\lambda=0}^{\infty}\cos\left[\sqrt{\kappa\lambda}(x-\xi)\right]\cos\left[\lambda(y-\eta)\right]e^{\lambda z}\,d\lambda\,d\xi\,d\eta \qquad (3.1)$$

Here, referring to Figure 3.1, Φ is the velocity potential in the fluid region $z \le 0$. γ_y is the unknown transverse (y-directed) vortex density component on the planing surface. The companion axial vortex density component, γ_x, is the usual subject of the conventional zero gravity slender body formulation of planing, but the two components are related by the condition of zero divergence of the two dimensional surface vector.

κ in equation (3.1) is the wave number $\kappa \equiv g/U^2$ and is present from the derivation of equation (3.1) in satisfying the linearized free surface boundary condition, allowing for gravity wave generation.

Note from equation (3.1) that only the sections at $\xi < x$ upstream convect into the current x-solution section; γ_y for $\xi < x$ will always be known from upstream computation steps. This x-marching characteristic of elliptic solutions in the y-coordinate system is common to the parabolic reduction in x associated with all slender body theories.

The linearized kinematic boundary condition on the $z = 0$ planing surface is:

$$\frac{\partial \Phi}{\partial z} = U \frac{\partial z_0}{\partial x} \quad \text{on } z = 0,\ -Y(x) \le x \le Y(x),\ 0 \le x \le L \tag{3.2}$$

Here, $z_0(x,y)$ is the definition of the planing surface $z - z_0(x, y) = 0$, which is presumed to be known.

Non-dimensionalize velocities on U and dimensions on the transom chine-half-beam Y_{ch}, and denote derivatives by subscripts. Equation (3.2) with equation (3.1) becomes:

$$z_{0x}(x, y) = \frac{1}{\pi} \int_{\eta=-Y(x)}^{Y(x)} \int_{\xi=0}^{x} \gamma_y(\xi,\eta) \int_{\lambda=0}^{\infty} \cos\left[\frac{\sqrt{\lambda}}{F_n}(x-\xi)\right] \cos[\lambda(y-\eta)]\lambda d\lambda\, d\xi\, d\eta \tag{3.3}$$

on $z = 0$. With this non-dimensionalization, the Froude number appearing in equation (3.3) is:

$$F_n \equiv \frac{U}{\sqrt{gY_{ch}}} \tag{3.4}$$

Since the boundary conditions are being satisfied on the $z = 0$ plane, z is set to zero in equation (3.3). However, while the resulting equation can then be integrated in terms of special functions, a non-obvious essential singularity results in the 2-D sectional-y solutions that produces non-convergent results. Maruo (1967) very indirectly implied recognition of this difficulty in his general formulation. Later, Tuck (1975), pursued Maruo's integral equation. Tuck recognized the singularity problem and showed it very succinctly, but was still not satisfied that he had dealt with it effectively in achieving stable, convergent numerical predictions. Vorus (April 2005) developed a general solution but admitted to needing further development. Later, Vorus and Taravella (2008) further refined the procedure which is derived below.

3.1.1 Mathematical Formulation

Redefine η and y of equation (3.1) as dimensionless on $Y(x)$ in order to create a rectangular grid:

$$z_{0x}(x,y)=\frac{Y(x)}{\pi}\int_{\eta=-1}^{1}\int_{\xi=0}^{x}\gamma_y(\xi,\eta)\int_{\lambda=0}^{\infty}\cos\left[\frac{\sqrt{\lambda}}{F_n}(x-\xi)\right]\cos[\lambda Y(x)(y-\eta)]\lambda d\lambda d\xi d\eta \tag{3.5}$$

Redefine λ as $\nu(x) = Y(x)\lambda$. Then, equation (3.5) becomes:

$$z_{0x}(x,y)=\frac{1}{\pi Y(x)}\int_{\eta=-1}^{1}\int_{\xi=0}^{x}\gamma_y(\xi,\eta)\int_{\nu=0}^{\infty}\cos\left[\sqrt{\frac{\nu}{Y(x)}}\frac{(x-\xi)}{F_n}\right]\cos[\nu(y-\eta)]\nu\, d\nu d\xi d\eta \tag{3.6}$$

Integrate piecewise in ξ over the currently active nx elements; $nx \le Nx$:

$$z_{0x}(x,y)=-\frac{F_n}{\pi\sqrt{Y(x)}}\sum_{i=1}^{nx}\int_{\nu=0}^{\infty}\sin\left[\sqrt{\frac{\nu}{Y(x)}}\frac{(x-\xi)}{F_n}\right]_{\xi_i}^{\xi_{i+1}}\int_{\eta=-1}^{1}\bar{\gamma}_{yi}(\eta)\cos[\nu(y-\eta)]\sqrt{\nu}\, d\eta d\nu \tag{3.7}$$

The x, ξ discretization is numbered with element i bounded by points i and i+1 and $x_1 = 0$. nx elements gives the terminal point as $i = nx$+1. By definition of the derivative:

$$\sin\left(\sqrt{\frac{\nu}{Y(x)}}\frac{(x-\xi)}{F_n}\right)\Bigg|_{\xi_i}^{\xi_{i+1}}=\Delta\xi_i\frac{\left[\sin\left(\sqrt{\frac{\nu}{Y(x)}}\frac{(x-\xi_{i+1})}{Fn}\right)-\sin\left(\sqrt{\frac{\nu}{Y(x)}}\frac{(x-\xi_i)}{Fn}\right)\right]}{\Delta\xi_i} \tag{3.8}$$

Take the limit as $\Delta\xi_i$ goes to zero:

$$\Delta\xi_i\frac{\partial}{\partial\xi_i}\sin\left(\sqrt{\frac{\nu}{Y(x)}}\frac{(x-\xi_i)}{F_n}\right)=-\frac{\Delta\xi_i}{Fn}\sqrt{\frac{\nu}{Y(x)}}\cos\left(\sqrt{\frac{\nu}{Y(x)}}\frac{(x-\xi_i)}{Fn}\right) \tag{3.9}$$

With substitution, equation (3.7) becomes:

$$z_{0x}(x,y)Y(x)=\frac{1}{\pi}\sum_{i=1}^{nx}\int_{\nu=0}^{\infty}\cos\left[\sqrt{\frac{\nu}{Y(x)}}\frac{(x-\bar{\xi}_i)}{F_n}\right]\Delta\xi_i\int_{\eta=-1}^{1}\bar{\gamma}_{yi}(\eta)\cos[\nu(y-\eta)]\nu\, d\eta d\nu \tag{3.10}$$

Where $\bar{\xi}_i = \frac{1}{2}(\xi_i + \xi_{i+1})$ and with $x \equiv \xi_{nx+1}$ equation (3.10) becomes:

$$z_{0x}(x,y)Y(x) = \frac{1}{\pi}\int_{\nu=0}^{\infty}\cos\left[\sqrt{\frac{\nu}{Y(x)}}\frac{\frac{1}{2}\Delta\xi_{nx}}{F_n}\right]\Delta\xi_{nx}\int_{\eta=-1}^{1}\bar{\gamma}_{ynx}(\eta)\cos[\nu(y-\eta)]d\nu\, d\eta d\nu$$

$$+\frac{1}{\pi}\sum_{i=1}^{nx-1}\int_{\nu=0}^{\infty}\cos\left[\sqrt{\frac{\nu}{Y(x)}}\frac{(x-\bar{\xi}_i)}{F_n}\right]\Delta\xi_i\int_{\eta=-1}^{1}\bar{\gamma}_{yi}(\eta)\cos[\nu(y-\eta)]d\nu\, d\eta d\nu \tag{3.11}$$

Now redefine the solution argument as:

$$\Delta\xi_i\bar{\gamma}_{yi} \equiv \frac{\Delta G_i}{2} \tag{3.12}$$

The argument of the cosine in the first term of equation (3.11) is small such that equations (3.11) and (3.12) are:

$$z_{0x}(x,y)Y(x) = \frac{1}{2\pi}\int_{\eta=-1}^{1}\Delta G_{nx}(\eta)\int_{\nu=0}^{\infty}\frac{\partial}{\partial y}\sin[\nu(y-\eta)]d\nu d\eta \tag{3.13}$$

$$+\frac{1}{2\pi}\sum_{i=1}^{nx-1}\int_{\nu=0}^{\infty}\cos\left[\sqrt{\frac{\nu}{Y(x)}}\frac{(x-\bar{\xi}_i)}{F_n}\right]\int_{\eta=-1}^{1}\Delta G_i(\eta)\frac{\partial}{\partial y}\sin[\nu(y-\eta)]d\nu d\eta$$

Exchange differentiation in y for differentiation in η:

$$z_{0x}(x,y)Y(x) = -\frac{1}{2\pi}\int_{\eta=-1}^{1}\Delta G_{nx}(\eta)\int_{\nu=-1}^{\infty}\frac{\partial}{\partial \eta}\sin[\nu(y-\eta)]d\nu d\eta$$

$$-\frac{1}{2\pi}\sum_{i=1}^{nx-1}\int_{\nu=0}^{\infty}\cos\left[\sqrt{\frac{\nu}{Y(x)}}\frac{(x-\bar{\xi}_i)}{F_n}\right]\int_{\eta=-1}^{1}\Delta G_i(\eta)\frac{\partial}{\partial \eta}\sin[\nu(y-\eta)]d\nu d\eta \tag{3.14}$$

Use Maruo's (1967) improper integral definition:

$$\frac{\partial}{\partial\eta}\int_{\nu=0}^{\infty}\sin\nu(y\pm\eta)d\nu = \mp\frac{\partial}{\partial\eta}\frac{1}{y\pm\eta}\cos\nu(y\pm\eta)\Big|_{\nu=0}^{\infty} = \pm\frac{\partial}{\partial\eta}\frac{1}{y\pm\eta} \tag{3.15}$$

(Here $e^{-\infty\frac{z}{Y}}\cos\infty(y\pm\eta)$ is taken as zero for arbitrarily small z).

Equation (3.14) can be written with variable change $\nu = \zeta^2$ in the 2nd integral of equation (3.14):

$$z_{0x}(x,y)Y(x) = -\frac{1}{2\pi}\int_{\eta=-1}^{1}\Delta G_{nx}(\eta)\frac{\partial}{\partial\eta}\frac{1}{y-\eta}d\eta$$

$$-\frac{1}{\pi}\sum_{i=1}^{nx-1}\int_{\eta=-1}^{1}\Delta G_i(\eta)\frac{\partial}{\partial\eta}\int_{\zeta=0}^{\infty}\zeta\cos(2b_i\zeta)\sin(a\zeta^2)\,\mathrm{sgn}(y-\eta)d\zeta d\eta \qquad (3.16)$$

where: $b_i = \dfrac{x-\bar{\xi}_i}{2F_n\sqrt{Y(x)}}$, $\qquad a = |y-\eta|$

The ζ-integral in equation (3.16) can be performed using integral formula 3.851.2 of Gradshteyn and Ryzhik (2000):

$$I_\zeta \equiv \int_{\zeta=0}^{\infty}\zeta\cos(2b_i\zeta)\sin(a\zeta^2)d\zeta =$$
$$\frac{\mathrm{sgn}(y-\eta)}{2a} - \frac{b_i}{a}\sqrt{\frac{\pi}{2a}}\left[\sin\left(\frac{b_i^2}{a}\right)C\left(\frac{b_i}{\sqrt{a}}\right) - \cos\left(\frac{b_i^2}{a}\right)S\left(\frac{b_i}{\sqrt{a}}\right)\right]\mathrm{sgn}(y-\eta) \qquad (3.17)$$

where C and S are Fresnel integrals for sine and cosine (Abramowitz and Stegun, 1964), respectively.

Return to equation (3.16):

$$z_{0x}(x,y)Y(x) = -\frac{1}{2\pi}\int_{\eta=-1}^{1}\Delta G_{nx}(\eta)\frac{\partial}{\partial\eta}\frac{1}{y-\eta}d\eta - \frac{1}{2\pi}\sum_{i=1}^{nx-1}\int_{\eta=-1}^{1}\Delta G_i(\eta)\frac{\partial}{\partial\eta}\left\{\frac{1}{y-\eta}\right.$$

$$\left.-\sqrt{2\pi}b_i\frac{1}{|y-\eta|^{3/2}}\left[\sin\left(\frac{b_i^2}{|y-\eta|}\right)C\left(\frac{b_i}{\sqrt{|y-\eta|}}\right) - \cos\left(\frac{b_i^2}{|y-\eta|}\right)S\left(\frac{b_i}{\sqrt{|y-\eta|}}\right)\right]\right\}d\eta \qquad (3.18)$$

where the circulation at x: $G_{nx}(y) = \sum_{i=1}^{nx}\Delta G_i(y)$.

Note that for the infinite F_n case, $b_i = 0$ in equation (3.18) and the first two terms coalesce to:

$$z_{0x}(x,y)Y(x) = -\frac{1}{2\pi}\int_{\eta=-1}^{1} G_{nx}(\eta)\frac{\partial}{\partial\eta}\frac{1}{y-\eta}d\eta \tag{3.19}$$

In equation (3.18), using the product rule:

$$\Delta G_i(\eta)\frac{\partial F(\eta)}{\partial\eta} = -F(\eta)\frac{\partial\Delta G_i(\eta)}{\partial\eta} + \frac{\partial}{\partial\eta}\left[\Delta G_i(\eta)F(\eta)\right] \tag{3.20}$$

with $\frac{\partial\Delta G_i}{\partial\eta} \equiv 2\Delta\gamma_{xi}(\eta)$, which is the complimentary axial vortex density distribution at *i*.

Further,

$$\int_{\eta=-1}^{1}\frac{\partial}{\partial\eta}(G_i F)d\eta = G_i F\Big|_{\eta=-1}^{1} = 0 \tag{3.21}$$

since $G_i(1) = \Delta G_i(-1) = 0$ by definition of the circulation.

Equation (3.18) becomes:

$$z_{0x}(x,y)Y(x) = \frac{1}{\pi}\int_{\eta=-1}^{1}\frac{\Delta\gamma_{x\,nx}(\eta)}{y-\eta}d\eta + \frac{1}{\pi}\sum_{i=1}^{nx-1}\int_{\eta=-1}^{1}\Delta\gamma_{xi}(\eta)\left\{\frac{1}{y-\eta}\right.$$

$$\left. -\sqrt{2\pi}b_i\frac{1}{|y-\eta|^{3/2}}\left[\sin\left(\frac{b_i^2}{|y-\eta|}\right)C\left(\frac{b_i}{\sqrt{|y-\eta|}}\right) - \cos\left(\frac{b_i^2}{|y-\eta|}\right)S\left(\frac{b_i}{\sqrt{|y-\eta|}}\right)\right]\right\}d\eta \tag{3.22}$$

For convenience, in later numerical analysis, collapse equation (3.22) with the field points on the positive axis.

$$z_{0x}(x,y)Y(x)=\frac{1}{\pi}\int_{\eta=0}^{1}\Delta\gamma_{x\,nx}(\eta)\left(\frac{1}{y-\eta}-\frac{1}{y+\eta}\right)d\eta \tag{3.23}$$

$$+\frac{1}{\pi}\sum_{i=1}^{nx-1}\int_{\eta=0}^{1}\Delta\gamma_{xi}(\eta)\left\{\frac{1}{y-\eta}-\sqrt{2\pi}b_i\frac{1}{|y-\eta|^{3/2}}\left[\sin\left(\frac{b_i^2}{|y-\eta|}\right)C\left(\frac{b_i}{\sqrt{|y-\eta|}}\right)-\cos\left(\frac{b_i^2}{|y-\eta|}\right)S\left(\frac{b_i}{\sqrt{|y-\eta|}}\right)\right]\right\}d\eta$$

$$-\frac{1}{\pi}\sum_{i=1}^{nx-1}\int_{\eta=0}^{1}\Delta\gamma_{xi}(\eta)\left\{\frac{1}{y-\eta}-\sqrt{2\pi}b_i\frac{1}{|y+\eta|^{3/2}}\left[\sin\left(\frac{b_i^2}{|y+\eta|}\right)C\left(\frac{b_i}{\sqrt{|y+\eta|}}\right)-\cos\left(\frac{b_i^2}{|y+\eta|}\right)S\left(\frac{b_i}{\sqrt{|y+\eta|}}\right)\right]\right\}d\eta$$

Now assume that $\Delta\gamma_{xi}$, $C\left(\frac{b_i}{\sqrt{|y-\eta|}}\right), S\left(\frac{b_i}{\sqrt{|y-\eta|}}\right), C\left(\frac{b_i}{\sqrt{|y+\eta|}}\right)$ and $S\left(\frac{b_i}{\sqrt{|y+\eta|}}\right)$ are

constant over a piecewise integration from n_j to n_{j+1}. Equation (3.23) becomes:

$$z_{0x}(x,y)Y(x)=\frac{1}{\pi}\int_{\eta=0}^{1}\Delta\gamma_{x\,nx}(\eta)\left(\frac{1}{y-\eta}-\frac{1}{y+\eta}\right)d\eta+\frac{1}{\pi}\sum_{i=1}^{nx-1}\left\{\int_{\eta=0}^{1}\Delta\gamma_{xi}(\eta)\left(\frac{1}{y-\eta}-\frac{1}{y+\eta}\right)d\eta\right.$$

$$-\sqrt{2\pi}\sum_{j=1}^{Ny}\Delta\gamma_{xi}(\overline{\eta})b_iC\left(\frac{b_i}{\sqrt{|y-\overline{\eta}_j|}}\right)\int_{\eta_j}^{\eta_{j+1}}\frac{1}{|y-\eta|^{3/2}}\sin\left(\frac{b_i^2}{|y-\eta|}\right)d\eta$$

$$+\sqrt{2\pi}\sum_{j=1}^{Ny}\Delta\gamma_{xi}(\overline{\eta})b_iS\left(\frac{b_i}{\sqrt{|y-\overline{\eta}_j|}}\right)\int_{\eta_j}^{\eta_{j+1}}\frac{1}{|y-\eta|^{3/2}}\cos\left(\frac{b_i^2}{|y-\eta|}\right)d\eta$$

$$+\sqrt{2\pi}\sum_{j=1}^{Ny}\Delta\gamma_{xi}(\overline{\eta})b_iC\left(\frac{b_i}{\sqrt{|y+\overline{\eta}_j|}}\right)\int_{\eta_j}^{\eta_{j+1}}\frac{1}{|y+\eta|^{3/2}}\sin\left(\frac{b_i^2}{|y+\eta|}\right)d\eta$$

$$\left.-\sqrt{2\pi}\sum_{j=1}^{Ny}\Delta\gamma_{xi}(\overline{\eta})b_iS\left(\frac{b_i}{\sqrt{|y+\overline{\eta}_j|}}\right)\int_{\eta_j}^{\eta_{j+1}}\frac{1}{|y+\eta|^{3/2}}\cos\left(\frac{b_i^2}{|y+\eta|}\right)d\eta\right\} \tag{3.24}$$

where

$$\overline{\eta}_j=\frac{\eta_{j+1}+\eta_j}{2} \tag{3.25}$$

Using the following integral formulas from *Mathematica* (2008):

$$\int \frac{1}{u^{3/2}} \sin\left(\frac{b^2}{u}\right) du = -\frac{\sqrt{2\pi}}{b} S\left(\frac{b}{\sqrt{u}}\right) \tag{3.26}$$

$$\int \frac{1}{u^{3/2}} \cos\left(\frac{b^2}{u}\right) du = -\frac{\sqrt{2\pi}}{b} C\left(\frac{b}{\sqrt{u}}\right) \tag{3.27}$$

equation (3.24) becomes

$$\begin{aligned} z_{0x}(x,y)Y(x) = {} & \frac{1}{\pi} \int_{\eta=0}^{1} \Delta\gamma_{x\,nx}(\eta)\left(\frac{1}{y-\eta} - \frac{1}{y+\eta}\right) d\eta + \frac{1}{\pi} \sum_{i=1}^{nx-1} \left\{ \int_{\eta=0}^{1} \Delta\gamma_{x\,i}(\eta)\left(\frac{1}{y-\eta} - \frac{1}{y+\eta}\right) d\eta \right. \\ & - 2\pi \sum_{j=1}^{Ny} \Delta\gamma_{xi}(\overline{\eta}_j) C\left(\frac{b_i}{\sqrt{|y-\overline{\eta}_j|}}\right) \left[S\left(\frac{b_i}{\sqrt{|y-\eta_{j+1}|}}\right) - S\left(\frac{b_i}{\sqrt{|y-\eta_j|}}\right) \right] \\ & + 2\pi \sum_{j=1}^{Ny} \Delta\gamma_{xi}(\overline{\eta}_j) S\left(\frac{b_i}{\sqrt{|y-\overline{\eta}_j|}}\right) \left[C\left(\frac{b_i}{\sqrt{|y-\eta_{j+1}|}}\right) - C\left(\frac{b_i}{\sqrt{|y-\eta_j|}}\right) \right] \\ & - 2\pi \sum_{j=1}^{Ny} \Delta\gamma_{xi}(\overline{\eta}_j) C\left(\frac{b_i}{\sqrt{|y+\overline{\eta}_j|}}\right) \left[S\left(\frac{b_i}{\sqrt{|y+\eta_{j+1}|}}\right) - S\left(\frac{b_i}{\sqrt{|y+\eta_j|}}\right) \right] \\ & \left. + 2\pi \sum_{j=1}^{Ny} \Delta\gamma_{xi}(\overline{\eta}_j) S\left(\frac{b_i}{\sqrt{|y+\overline{\eta}_j|}}\right) \left[C\left(\frac{b_i}{\sqrt{|y+\eta_{j+1}|}}\right) - C\left(\frac{b_i}{\sqrt{|y+\eta_j|}}\right) \right] \right\} \end{aligned} \tag{3.28}$$

with

$$b_i = \frac{x - \overline{\xi}_i}{2F_n \sqrt{Y_{nx+1}}} \tag{3.29}$$

3.1.2 Numerical Analysis

Considering that all of the $\Delta\gamma_{xi}$ for $i < nx$ are known from upstream steps, write equation (3.28) for solution as:

$$z_{0x}(x,y)Y(x) = \frac{1}{\pi}\int_{\eta=0}^{1}\Delta\gamma_{x\,nx}(\eta)\left(\frac{1}{y-\eta}-\frac{1}{y+\eta}\right)d\eta + R_{nx-1}(y) \tag{3.30}$$

with:

$$\begin{aligned}
R_{nx-1}(y) = \frac{1}{\pi}\sum_{i=1}^{nx-1}\Bigg\{ & \int_{\eta=0}^{1}\Delta\gamma_{x\,i}(\eta)\left(\frac{1}{y-\eta}-\frac{1}{y+\eta}\right)d\eta \\
& -2\pi\sum_{j=1}^{Ny}\Delta\gamma_{xi}(\overline{\eta}_j)C\left(\frac{b_i}{\sqrt{|y-\overline{\eta}_j|}}\right)\left[S\left(\frac{b_i}{\sqrt{|y-\eta_{j+1}|}}\right)-S\left(\frac{b_i}{\sqrt{|y-\eta_j|}}\right)\right] \\
& +2\pi\sum_{j=1}^{Ny}\Delta\gamma_{xi}(\overline{\eta}_j)S\left(\frac{b_i}{\sqrt{|y-\overline{\eta}_j|}}\right)\left[C\left(\frac{b_i}{\sqrt{|y-\eta_{j+1}|}}\right)-C\left(\frac{b_i}{\sqrt{|y-\eta_j|}}\right)\right] \\
& -2\pi\sum_{j=1}^{Ny}\Delta\gamma_{xi}(\overline{\eta}_j)C\left(\frac{b_i}{\sqrt{|y+\overline{\eta}_j|}}\right)\left[S\left(\frac{b_i}{\sqrt{|y+\eta_{j+1}|}}\right)-S\left(\frac{b_i}{\sqrt{|y+\eta_j|}}\right)\right] \\
& +2\pi\sum_{j=1}^{Ny}\Delta\gamma_{xi}(\overline{\eta}_j)S\left(\frac{b_i}{\sqrt{|y+\overline{\eta}_j|}}\right)\left[C\left(\frac{b_i}{\sqrt{|y+\eta_{j+1}|}}\right)-C\left(\frac{b_i}{\sqrt{|y+\eta_j|}}\right)\right]\Bigg\}
\end{aligned} \tag{3.31}$$

From equation (3.30):

$$C_{kj}\Delta\gamma_{xnxk} = z_{0xk} \tag{3.32}$$

The discretization is as follows:

1) The positive-side axis is divided into *Ny* elements with $\Delta y = 1/Ny$.

2) The j = 1, Ny points (η-pts) at the element ends, excluding the origin, are the locations of point vortices $\Delta\Gamma_{xij} = 2\Delta\gamma_{xij}\Delta y_j$

3) The k = 1, Ny points (y-pts) at the element centers are Ny field points where the kinematic boundary condition is satisfied.

$$z_{0xnx,k}Y_{nx,k} - R_{nx-1,k} = \sum_{j=1}^{Ny} C_{j,k}\Delta\Gamma_{xnx,j} \qquad k= 2, \ldots, Ny+1 \tag{3.33}$$

The point vortices are of strength $\Delta\Gamma_{nx,j} = 2\Delta\gamma_{nx,j}\Delta\ell$ where $\Delta\ell = 1/Ny$. From equation (3.30):

$$C_{j,k} = \frac{1}{2\pi}\left(\frac{1}{y_k - \eta_j} - \frac{1}{y_k + \eta_j}\right) \tag{3.34}$$

$$\begin{aligned} R_{nx-1,k} = \frac{1}{2\pi}\sum_{i=1}^{nx-1}\sum_{j=1}^{Ny}\Bigg\{ & \Delta\Gamma_{xi,j}\left(\frac{1}{y_k - \eta_j} - \frac{1}{y_k + \eta_j}\right) \\ & - 2\pi\frac{\Delta\Gamma_{xi,j}}{\Delta\ell}C\left(\frac{b_i}{\sqrt{|y_k - \overline{\eta}_j|}}\right)\left[S\left(\frac{b_i}{\sqrt{|y_k - \eta_{j+1}|}}\right) - S\left(\frac{b_i}{\sqrt{|y_k - \eta_j|}}\right)\right] \\ & + 2\pi\frac{\Delta\Gamma_{xi,j}}{\Delta\ell}S\left(\frac{b_i}{\sqrt{|y_k - \overline{\eta}_j|}}\right)\left[C\left(\frac{b_i}{\sqrt{|y_k - \eta_{j+1}|}}\right) - C\left(\frac{b_i}{\sqrt{|y_k - \eta_j|}}\right)\right] \\ & - 2\pi\frac{\Delta\Gamma_{xi,j}}{\Delta\ell}C\left(\frac{b_i}{\sqrt{|y_k + \overline{\eta}_j|}}\right)\left[S\left(\frac{b_i}{\sqrt{|y_k + \eta_{j+1}|}}\right) - S\left(\frac{b_i}{\sqrt{|y_k + \eta_j|}}\right)\right] \\ & + 2\pi\frac{\Delta\Gamma_{xi,j}}{\Delta\ell}S\left(\frac{b_i}{\sqrt{|y_k + \overline{\eta}_j|}}\right)\left[C\left(\frac{b_i}{\sqrt{|y_k + \eta_{j+1}|}}\right) - C\left(\frac{b_i}{\sqrt{|y_k + \eta_j|}}\right)\right]\Bigg\} \end{aligned} \tag{3.35}$$

Equation (3.33) is inverted for the point vortices with spreading back to vortex distribution by:

$$2\Delta\gamma_{nx,j} = \frac{\Delta\Gamma_{nx,j}}{\Delta\ell} \tag{3.36}$$

With $\gamma_x(x, y)$ now known, $\gamma_y(x, y)$ can be determined by:

$$\frac{\partial\gamma_x}{\partial x} + \frac{\partial\gamma_y}{\partial y} = 0 \tag{3.37}$$

The Bernoulli equation can now be used to give the planing surface pressure.

$$p(x, y, z) + \rho gz + \frac{1}{2}\rho\left\{\left[U + u(x, y)\right]^2 + v(x, y)^2 + w(x, y)^2\right\} = 0 \tag{3.38}$$

Linearize equation (3.38) and evaluate the result on $z = 0$.

$$p(x, y) = -\rho U u(x, y) \qquad \text{on } z = 0 \tag{3.39}$$

The coefficient of pressure difference across the surface is then:

$$C_p(x, y) = \frac{p(x, y)}{\frac{1}{2}\rho U^2} \tag{3.40}$$

Substitute equation (3.39) into equation (3.40):

$$C_p(x, y) = -2\left(\frac{u}{U}\right) \tag{3.41}$$

Considering all velocity quantities henceforth dimensionless on U, $u(x,y)$ is written on the planing surface in terms of vortex strength γ_y as:

$$u(x, y) = -\gamma_y(x, y) \tag{3.42}$$

The pressure coefficient is given in terms of equation (3.41), is then just:

$$C_p(x, y) = 2\gamma_y(x, y) \tag{3.43}$$

The sectional lift coefficient is given in terms of equation (3.43) as:

$$C_l \equiv \frac{l(x)}{\frac{1}{2}\rho U^2 Y(x)} = 2\int_{y=0}^{1} C_p(x, y)dy = 4\int_{y=0}^{1}\gamma_y(x, y)dy \tag{3.44}$$

The total lift coefficient is:

$$C_L \equiv \frac{L_F}{\frac{1}{2}\rho U^2 Y_{ch}^2} = \int_{x=0}^{L} C_l(x) Y(x) dx \tag{3.45}$$

The sectional drag is the sectional integral of the axial projection of the surface pressure:

$$C_d \equiv \frac{d(x)}{\frac{1}{2}\rho U^2 Y(x)} = 2\int_{y=0}^{1} C_p(x,y) z_{0x}(x,y) dy = 4\int_{y=0}^{1} \gamma_y(x,y) z_{0x}(x,y) dy \tag{3.46}$$

The total drag coefficient is:

$$C_D \equiv \frac{D}{\frac{1}{2}\rho U^2 Y_{ch}^2} = \int_{x=0}^{L} C_d(x) Y(x) dx \tag{3.47}$$

3.2 Results

The general formulation of the Maruo theory has been applied to a body whose projection on the z = 0 plane is a flat delta foil. It is applied to a low-aspect ration foil with a length-to-beam ratio of five as has been done on two previous occasions: Maruo (1967) and Tuck (1975). The triangular planing plate (or delta plate), Figure 3.2, therefore serves as a comparative basis for checking the general slender-body planing theory formulated in Section 3.1.

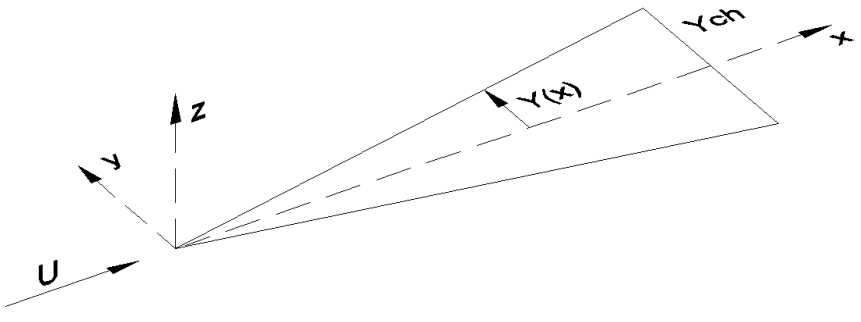

Figure 3.2 – Flat delta planing plate test model

Maruo (1967) never actually solved his integral equation; he said it was too difficult. Instead, Maruo produced an asymptotic approximation by requiring the Froude number to be very high: $\frac{1}{F_n}\sqrt{\frac{L}{Y_{ch}}} = O(1)$. This allowed Maruo to substitute the infinite Froude number solution, $\gamma_{fy}(x, y)$, by equation (3.19), with the full kernel of equation (3.3) to calculate the correction for wave effects.

Tuck (1975) did solve the full equation numerically, but he was pessimistic about his numerical analysis being poorly conditioned due to the higher order singular behavior in *y*. That appears to have led to some questionable predictions by Tuck (by his own admission).

As can be seen in Figures 3.3 through 3.5, Vorus and Taravella's (2009) general solution yields results comparable to Maruo (1967) and Tuck's (1975) for the flat delta foil. Variations of discretization were investigated by Xie (2005), who mentioned that Tuck (1975) and various others that attempted a solution to this problem required a coarse discretization in the transverse direction (i.e. limited to using less than five or six buttock lines). Xie (2005) noted that this is not due to the singularity in the problem, as was claimed by Maruo (1967), Tuck (1975) and Cole (1988). Rather it is due to the numerical accuracy (or lack thereof) of the methods used. Xie (2005) also mentioned that discretization, in these cases, should be chosen with speed in mind. It is noted that in his computed results, Tuck's (1975) finest grid is 20 by 20. It appears that Tuck (1975) did indeed use a coarser grid for lower speeds as Xie (2005) claimed, but the exact values of *Nx* and *Ny* are not evident for all of the cases presented.

With this in mind, Vorus and Taravella (2009) investigated the effects of the discretization on the numerical results. The results of their analysis are compared to Maruo (1967) and Tuck's (1975) results in Figures 3.3 to 3.6 for the delta plate.

For their numerical analysis, Vorus and Taravella (2009) chose to perform computations for the delta plate with a length to half-beam ratio (L/Y_{ch}) of 10 and a unit angle of attack ($\alpha = 1$ radian). Variations of the results are plotted for $60 \leq Nx \leq 100$ and $10 \leq Ny \leq 30$.

Figures 3.3 to 3.6 depicts the lift of the flat delta plate, scaled with respect to the zero gravity limit, and plotted against $\nu = gL^2 / U^2 B$. As can be easily seen from these figures, Vorus and Taravella's (2009) results compare quite nicely with Maruo (1967) and Tuck (1975). A close look at the curve of Vorus and Taravella (2009) shows that the slope of the lift curve as Froude number approaches infinity is zero. This result is physically realistic. It is not seen in the results of Maruo (1967) or Tuck (1975) to their order of approximation.

Figures 3.3 to 3.5 depict the affect of the selection of transverse discretization (i.e. *Ny*) on the results of Vorus and Taravella's (2009) general solution. For the plan forms studied, convergence was achieved around *Ny* = 30. However, when considering computational time, numerical accuracy (as compared to Maruo), and the pressure distribution analysis, *Ny* = 20 seems to offer the best results for this test case.

The results for *Ny* = 20 predicts about 2% less computed lift as opposed to the converged solution at *Ny* = 30. This is done at a fraction of the computational time. For *Ny* = 20, the algorithm has to solve a 20 x 20 system of linear equations for every station as opposed to a 30 x 30 or greater system of linear equations for every station. This cuts the computational time significantly. As will be discussed later, the pressure distributions begin to oscillate wildly for larger *Ny*.

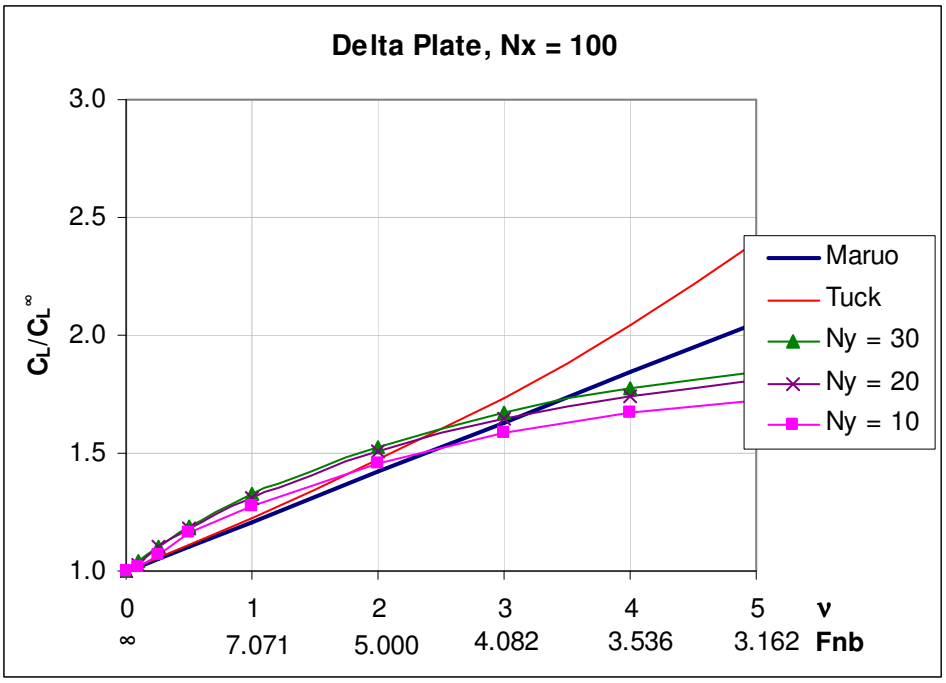

Figure 3.3 – Comparison of Vorus-Taravella's (2009) general solution with *Nx* = 100 to Maruo (1967) and Tuck (1975) for delta plate

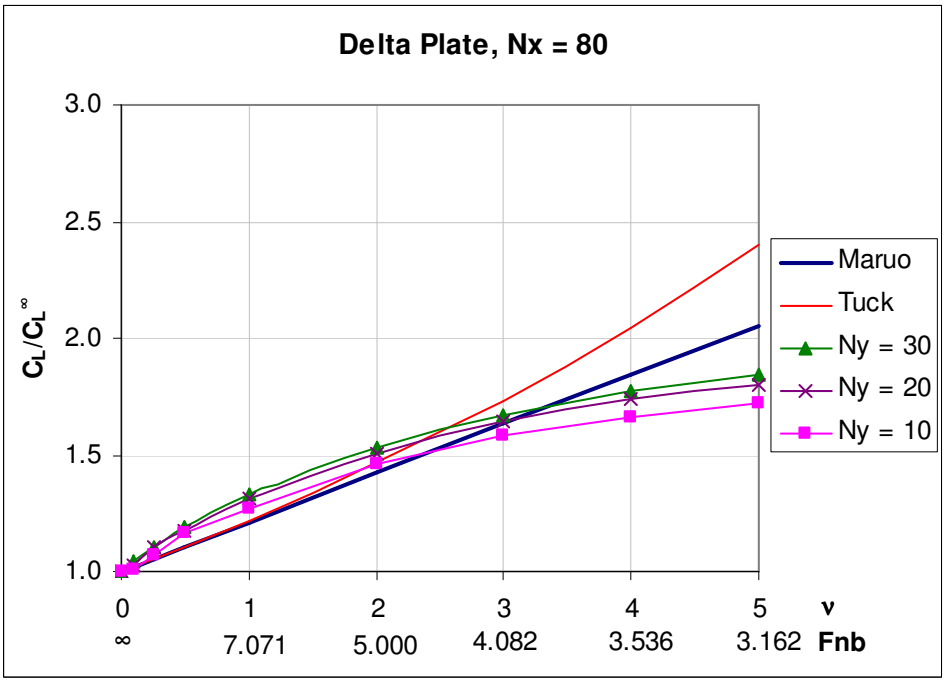

Figure 3.4 – Comparison of Vorus-Taravella's (2009) general solution with *Nx* = 80 to Maruo (1967) and Tuck (1975) for delta plate

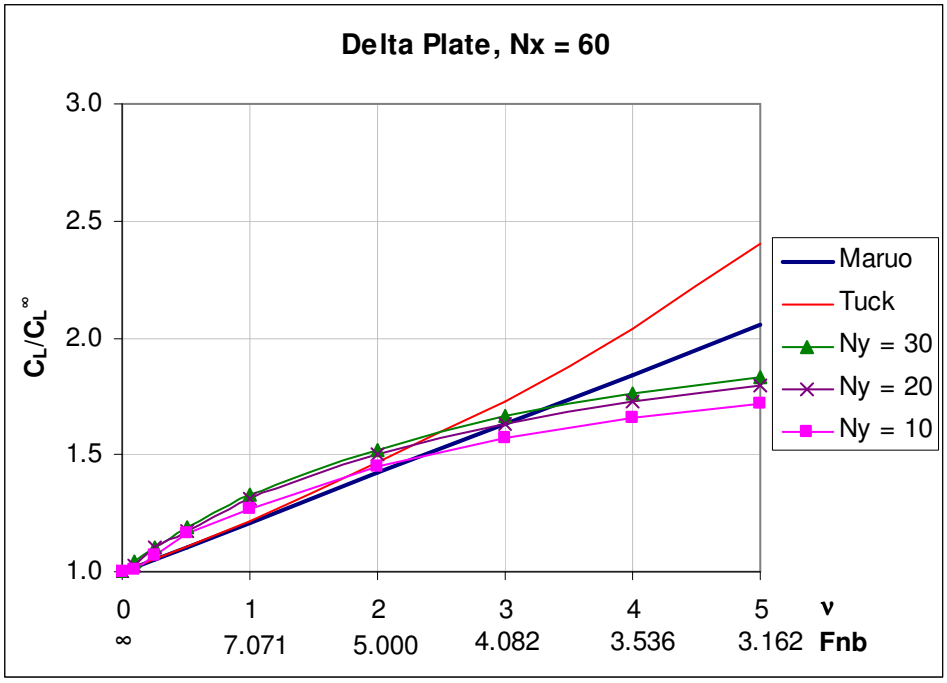

Figure 3.5 – Comparison of Vorus-Taravella's (2009) general solution with *Nx* = 60 to Maruo (1967) and Tuck (1975) for delta plate

Figure 3.6 depicts the results for varying *Nx*. The general solution presented in Section 3.1 is not nearly as sensitive to *Nx* as it is to *Ny*. As can be seen in the figure below, cutting the *x*-discretization nearly in half minimally affects the results.

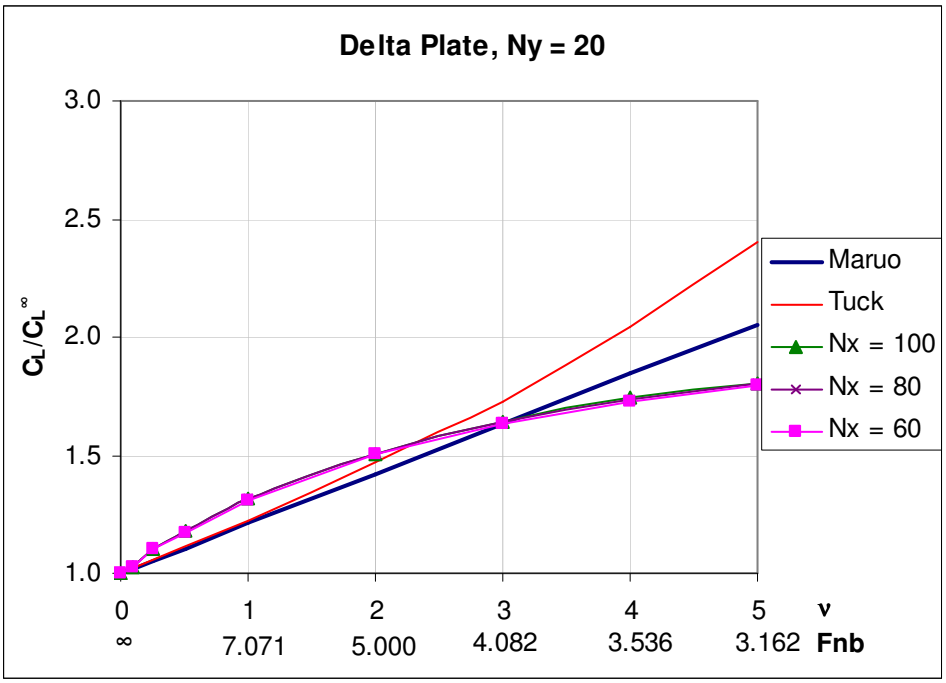

Figure 3.6 – Comparison of Vorus-Taravella's (2009) general solution with *Ny* = 20 to Maruo (1967) and Tuck (1975) for delta plate

Tuck's (1975) transverse pressure distributions indicate a centerplane singularity as Froude number decreases. He admitted to having numerical difficulty in this area, but he attributes this sharp pressure peak to the existence of a leading-edge spray sheet. Tuck's (1975) lack of confidence in his results, however, was mostly because he was calculating a negative pressure at the chine which implies a negative infinity in the pressure. Tuck claimed that this singularity seems not to be present in the physical problem.

The present pressure distribution results (Vorus and Taravella 2009) for the delta planing foil are shown in Figures 3.7 and 3.8. While the results indicate that gravity does have an effect on the centerline distribution at relatively low Froude numbers, they do not indicate that a centerline singularity is present as in Tuck (1975). Recall, that the infinite Froude number (zero gravity) distribution in *y* are semi-elliptical. There are also no negative edge loadings. It is noted, however, that when the *y*-discretization is increased beyond, say, *Ny* > 25, the transverse

pressure distributions begin to oscillate wildly, especially near the transom. While increasing *Ny* seems to offer the best comparison to Maruo's (1967) results in regards to total lift, increasing the *Ny* discretization predicts some unrealistic pressure distributions.

From Figure 3.7, one can see that the elliptical infinite Froude number (or zero gravity solution) is evident at the bow. The distributions depicted here do not become erratic in the first few stations as Tuck (1975) suggested occurred in his analysis. Rather, the oscillations slowly develop toward the transom while a zero pressure gradient is maintained across the centerplane of the vessel. Tuck (1975) computed a pressure singularity at the centerplane which he attributed to leading edge spray drag, but Tuck also mentions that this could be the result of inaccuracies of his program. This phenomenon is not evident in Vorus and Taravella's (2009) results presented below.

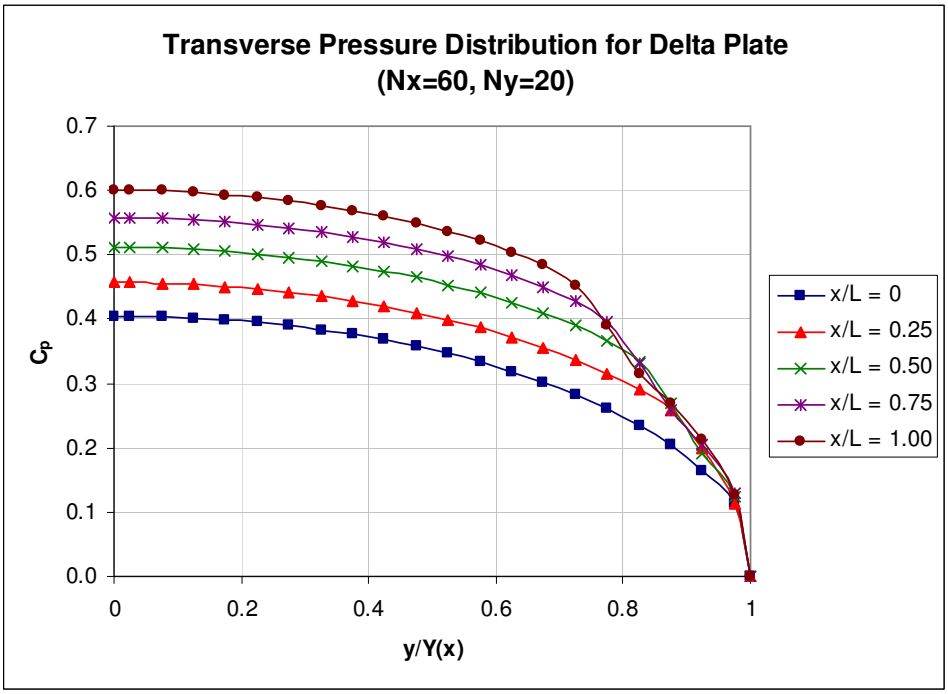

Figure 3.7 – Transverse pressure distribution at quarter stations for delta plate at $\nu = 1.25$ ($Nx = 60$, $Ny = 20$)

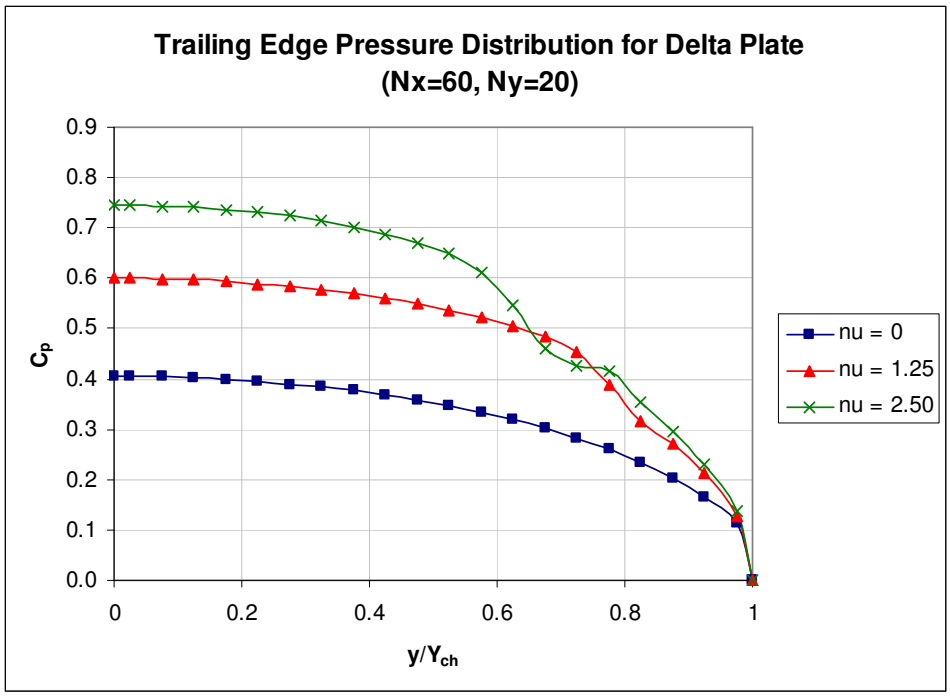

Figure 3.8 – Trailing edge pressure distribution at various ν for delta plate (*Nx* = 60, *Ny* = 20)

The oscillations seen in the pressure distributions above have been discussed by many authors in the past. Maruo (1967) claimed that the integral equation for low-aspect ratio lifting bodies is highly singular and will cause analytical and numerical difficulty. Tuck (1975) never seemed satisfied with his routine or results. He also agreed with Maruo that the equation was singular and he did offer some possible suggestions for addressing the singularity. Whether or not Tuck pursued these methods is unknown. Tuck (1975) also suggested that the oscillations in the pressure distribution are the result of short diverging waves and not entirely a numerical anomaly. Xie (2005) suggests that Tuck's (1975) problems were the result of numerical accuracy of his computer code, especially near the singularity, and not due to the theoretical formulation.

Vorus and Taravella (2009) believe that the oscillation of the pressure distribution is the result of physics as opposed to numerical accuracy. The singularity often discussed has been somewhat eliminated by integral equations (3.26) and (3.27). While the argument of the Fresnel integrals may be still be singular, both the sine and cosine Fresnel integrals approach 1/2 as the argument approaches infinity. Therefore, there is a limit. It is believed that the pressure oscillations can be initially attributed to the diverging wave system and exasperated by the numerical accuracy of the routine.

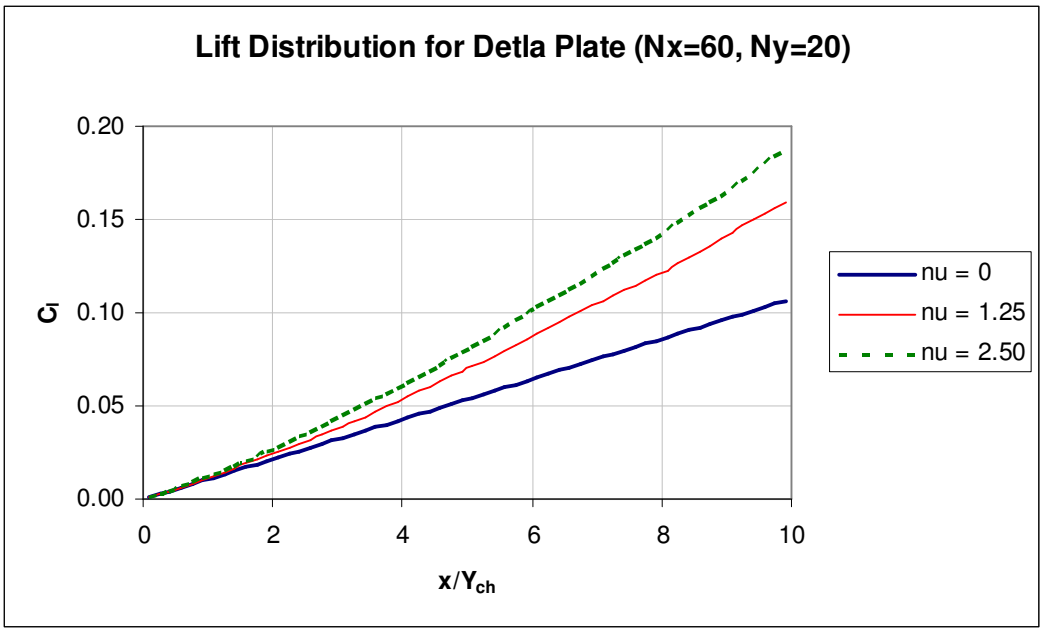

Figure 3.9 – Sectional lift coefficient distributions at various ν for delta plate (*Nx* = 60, *Ny* = 20)

In addition to the triangular waterplane, Tuck (1975) also presented results for a cusped waterplane. This waterplane is defined as:

$$y(x) = \left(\frac{Y_{ch}}{L^2}\right)x^2 \tag{3.48}$$

and is depicted in Figure 3.10.

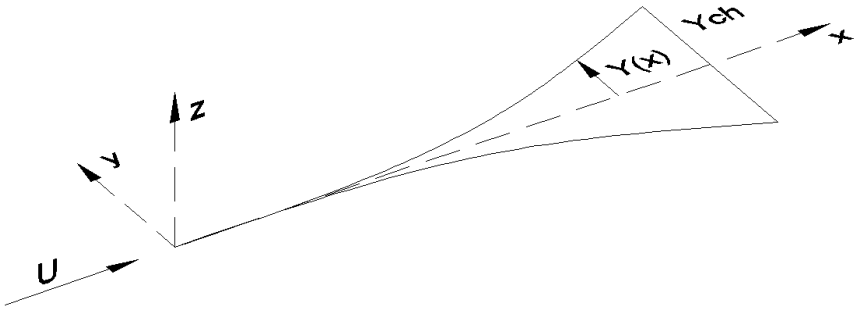

Figure 3.10 – Cusped planing plate test model

For further analysis and discussion, Vorus and Taravella (2009) also computed results for the cusped plate (of similar dimensions as the delta plate) using the general solution presented in section 3.1. These results were also compared to Tuck's (1975) analysis.

The results of the discretization analysis of the cusped plate yielded very similar results to that of the delta plate. The results reached convergence for $Nx = 60$ and $Ny = 30$; however, more realistic pressure distributions were obtained without sacrificing much precision (with regards to total lift) when $Ny = 20$.

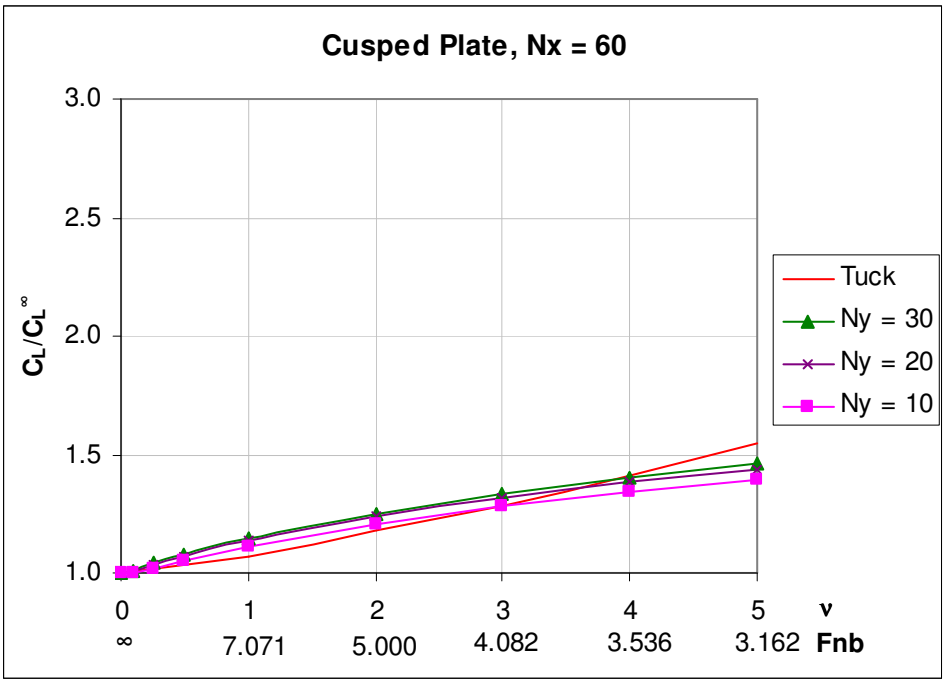

Figure 3.11 – Comparison of Vorus-Taravella's (2009) general solution with *Nx* = 60 to Tuck (1975) for cusped plate

The results of the transverse pressure distribution analysis are presented in Figure 3.12. For $\nu = 1.25$, the transverse pressure distribution remains somewhat elliptic. There are no oscillations in the transverse pressure distributions for the speeds covered in Figures 3.12 and 3.13. This is said to be due to the shape of the waterplane.

Similar results to the delta waterplane as for the cusped waterplane are achieved at the trailing edge. These results present more of an elliptic loading pattern as compared to those of Tuck (1975). For the results printed below, there are no obvious pressure oscillations; however, as the speed is further decreased, these oscillations will appear.

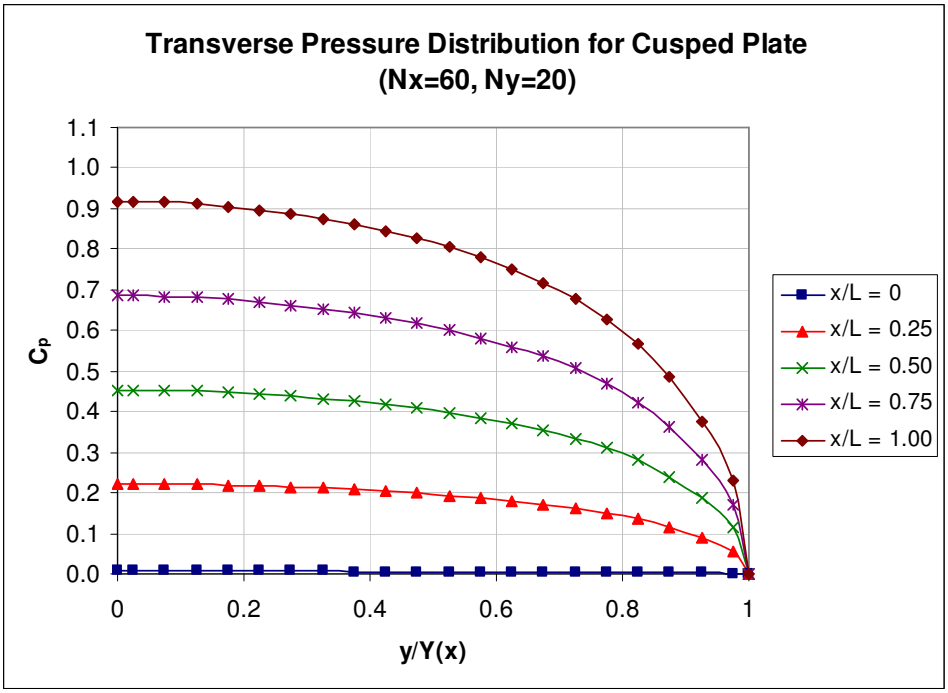

Figure 3.12 – Transverse pressure distribution at quarter stations for delta plate at $\nu = 1.25$ ($Nx = 60$, $Ny = 20$)

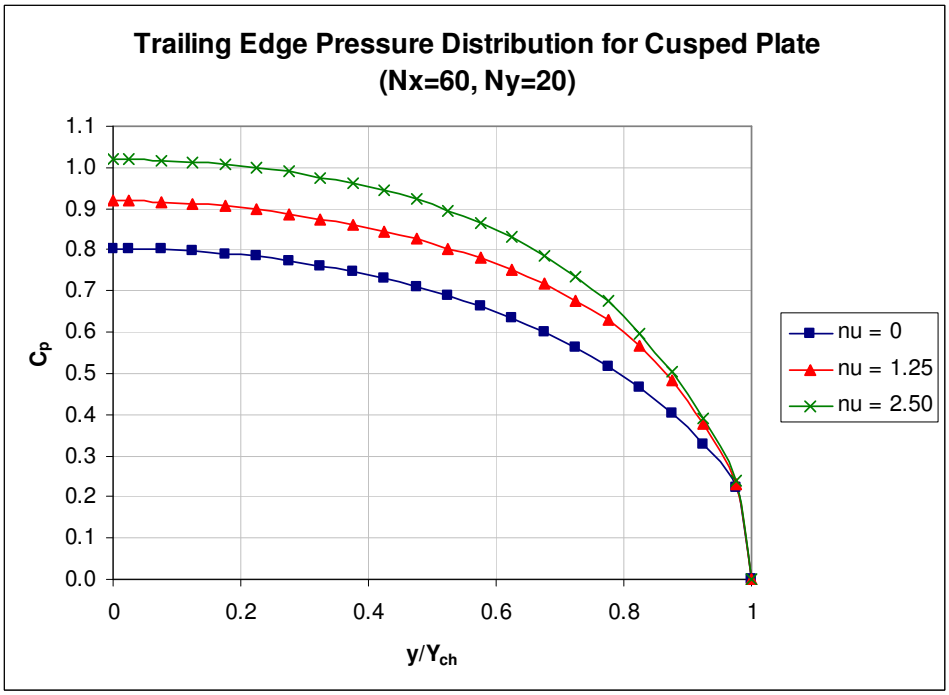

Figure 3.13 – Trailing edge pressure distribution at various ν for delta plate ($Nx = 60$, $Ny = 20$)

The sectional lift distribution for the cusped plate is depicted in Figure 3.14. As for the delta plate, the distribution is smooth with no erratic jumps or discontinuities. One can also observe that the center of lift moves toward the transom as the Froude number decreases. This effect is the result of the hull form obtaining additional dynamic lift from the waves that are being developed aft. This will make the selection of the stern lines of a slender semi-planing/semi-displacement hull form important when designing the hull form.

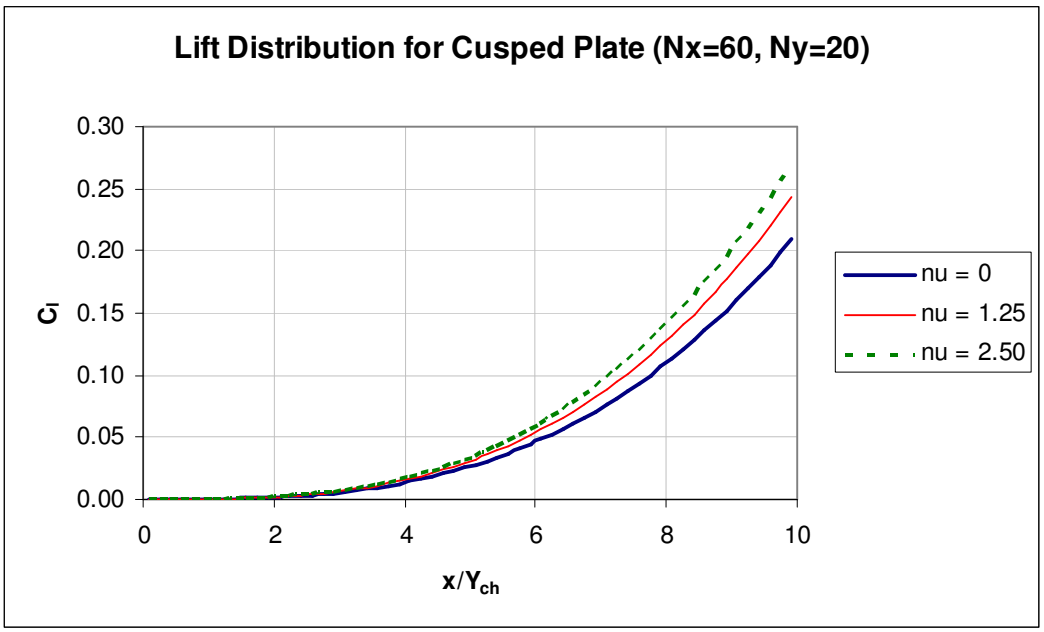

Figure 3.14 – Sectional lift coefficient distributions at various ν for cusped plate (*Nx* = 60, *Ny* = 20)

As shown from the results of the delta plate and the cusped plate presented in this section, Vorus and Taravella (2009) have produced an applicable general solution to Maruo's (1967) low aspect ratio planing problem. The effects of the infamous singularity have been eliminated. Vorus and Taravella (2009) obtained a reasonable comparison to Maruo (1967) for total lift and physically acceptable pressure distributions at high to moderate speeds. No centerline loading singularities or negative edge pressures were obtained using a reasonable discretization for an

appropriate speed range. Vorus and Taravella (2009) also achieved a convergent solution for total lift.

4.0 Application to Semi-Planing/Semi-Displacement Hulls

Application of the hybrid method will be completed for variations of a semi-hull which was originally described by Vorus (2005). While Vorus (2005) admitted to having some limitations to his method (mainly with high speed Michell's integral, wake trench determination and numerical difficulties with Maruo formulation), he was able to draw some very important conclusions with regard to hull form.

Improvements have been made in regards to the high speed Michell integral and the general solution for the Maruo integral by Vorus and Taravella (2008 and 2009) and presented in this work. The conclusions drawn by Vorus (2005) have been further investigated for the semi-hull with the current improvements to the hybrid method. Adjustments to various hull parameters are made and the effects on lift and drag are studied. Finally, recommendations will be made for optimization of the semihull.

4.1 Semi-hull Geometry Definition

The semihull is defined as a fine-formed, wave piercing, displacement bow with a flat, planing stern. The geometry of the semihull can be described by 12 main parameters as shown in Table 4.1 and Figures 4.1 through 4.3. The hull form is basically defined by the chine offset, deadrise angle distribution, and keel upset. The chine offset is defined as cubic a curve starting at the bow and transitioning into a straight line that is parallel to the centerline until it reaches the transom (see Figure 4.1). The deadrise angle distribution is defined, generally, as a cubic curve starting at the bow, and transitioning to a constant distribution for a given distance and then transitions into another cubic line until it reaches the transom (see Figure 4.2). The height of the

chine can be determined from the given chine offset, deadrise angle and draft at a given longitudinal position.

Table 4.1 – Twelve parameters that describe the Semihull

L	Length of waterline
Y_{ch}	Chine offset at transom
H_T	Transom draft
Y_{0x}	Slope of chine offset at entry
L_{ac}	Forward chine tangent point, forward from transom
β_0	Deadrise angle at entry
β_{0x}	Rate of change of deadrise angle at entry
β_{01}	Intermediate constant value of deadrise angle
β_1	Deadrise angle at transom
β_{1x}	Rate of change of deadrise angle at transom
L_{ab}	Forward deadrise tangent point, forward from transom
L_{bb}	Aft deadrise tangent point, forward from transom

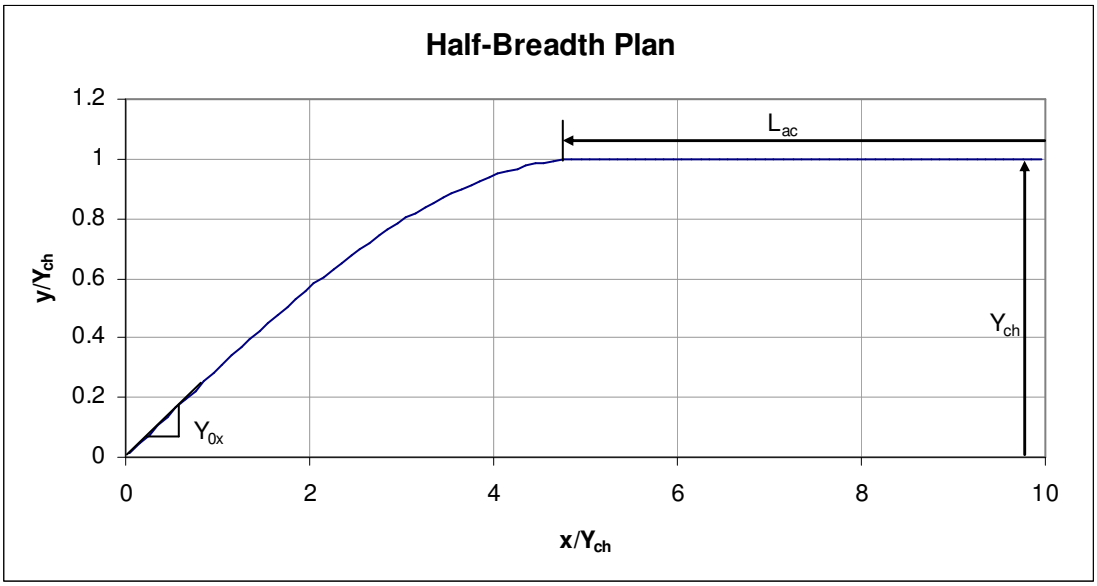

Figure 4.1 – Half-breadth plan depicting geometry components for the Semihull

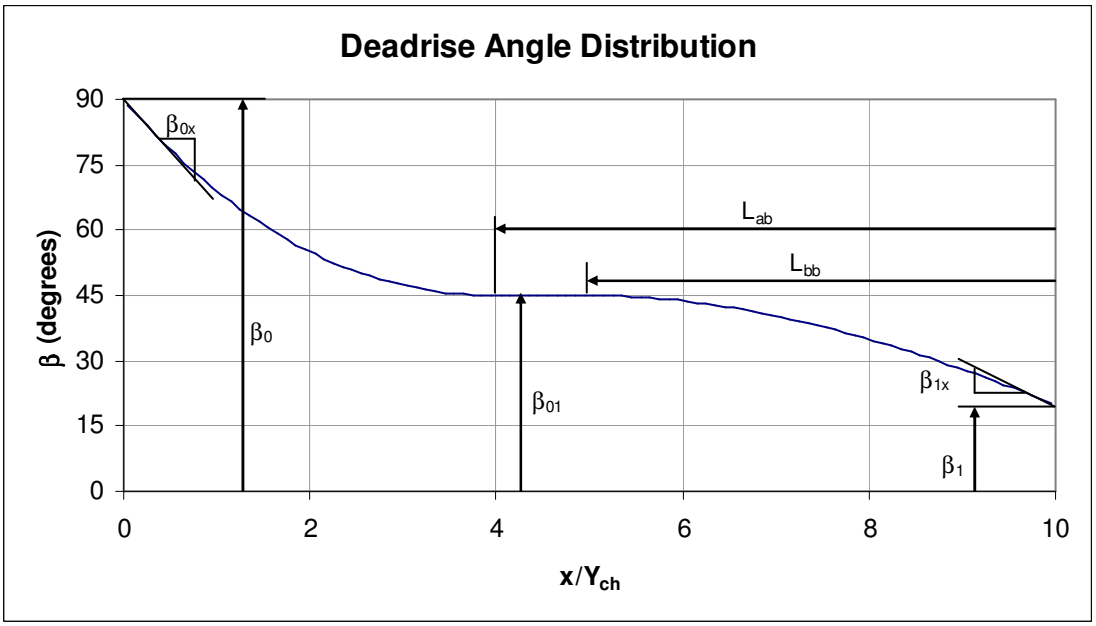

Figure 4.2 – Deadrise angle distribution depicting geometry components for the Semihull

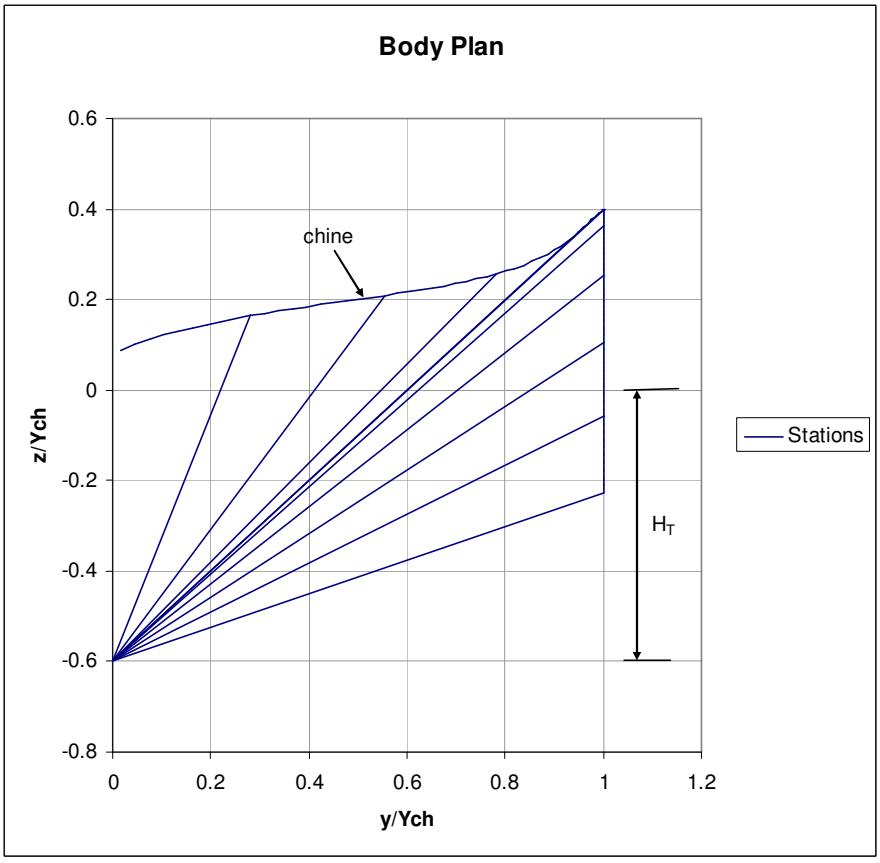

Figure 4.3 – Body plan depicting geometry components for the Semihull

4.2 Semihull 1 – Base Case

The evaluation of the prototype semihull using the present formulation has been completed as was done by Vorus (June 2005). Admittedly, the theory presented by Vorus (June 2005) was an initial attempt at the hybrid theory and there were some short comings in the components of the theory. The present evaluation will consider the modified Michell's integral for high speed and the Maruo general solution presented in this work.

The analysis completed by Vorus (June 2005) was done for a semihull with geometric parameters as shown in Table 4.2, a length of 196.85 ft (60 m) and a running speed of 50 knots (Fn = 1.060).

Table 4.2 – Semihull 1 geometric parameters

Length of waterline	L	10	
Chine offset at transom	Y_{ch}	1	
Transom draft	H_T	0.6	
Slope of chine offset at entry	Y_{0x}	0.3	
Forward chine tangent point, forward from transom	L_{ac}	5	
Deadrise angle at entry	β_0	90	deg.
Rate of change of deadrise angle at entry	β_{0x}	-25	deg./(ft/ft)
Intermediate constant value of deadrise angle	β_{01}	45	deg.
Deadrise angle at transom	β_1	20	deg.
Rate of change of deadrise angle at transom	β_{1x}	-8.5	deg./(ft/ft)
Forward deadrise tangent point, forward from transom	L_{ab}	6	
Aft deadrise tangent point, forward from transom	L_{bb}	5	

Figure 4.4 shows the running body plan and Figure 4.5 shows the running half breadth plan.

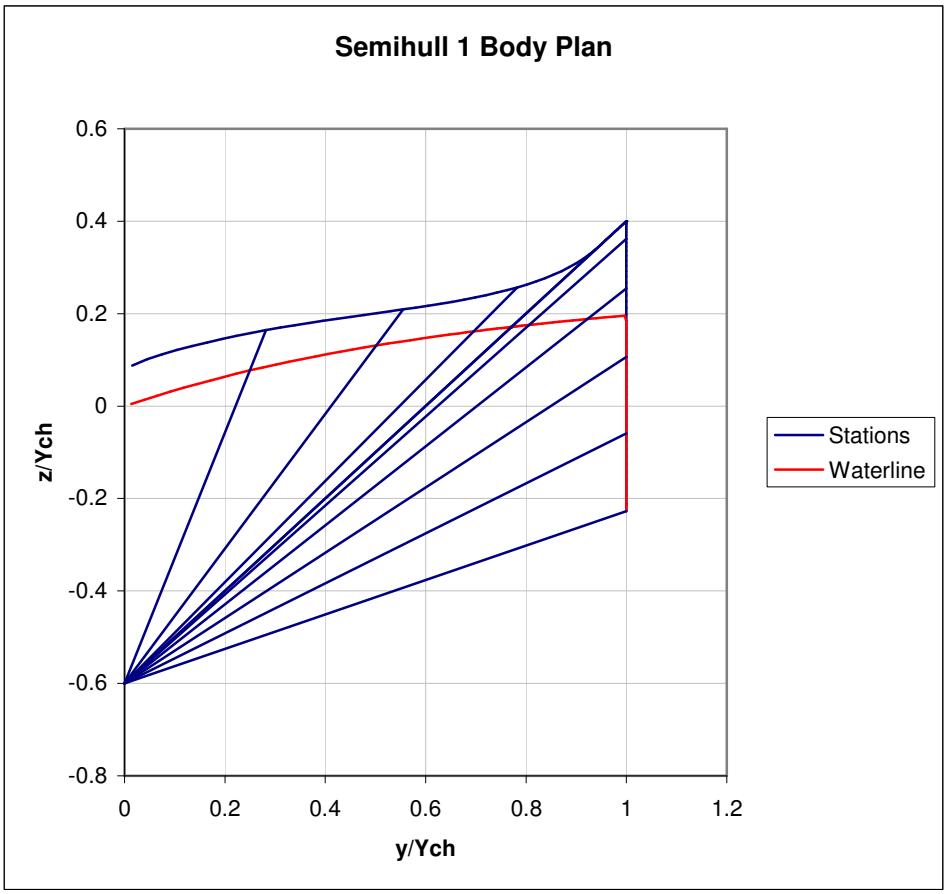

Figure 4.4 – Running body plan of Semihull 1

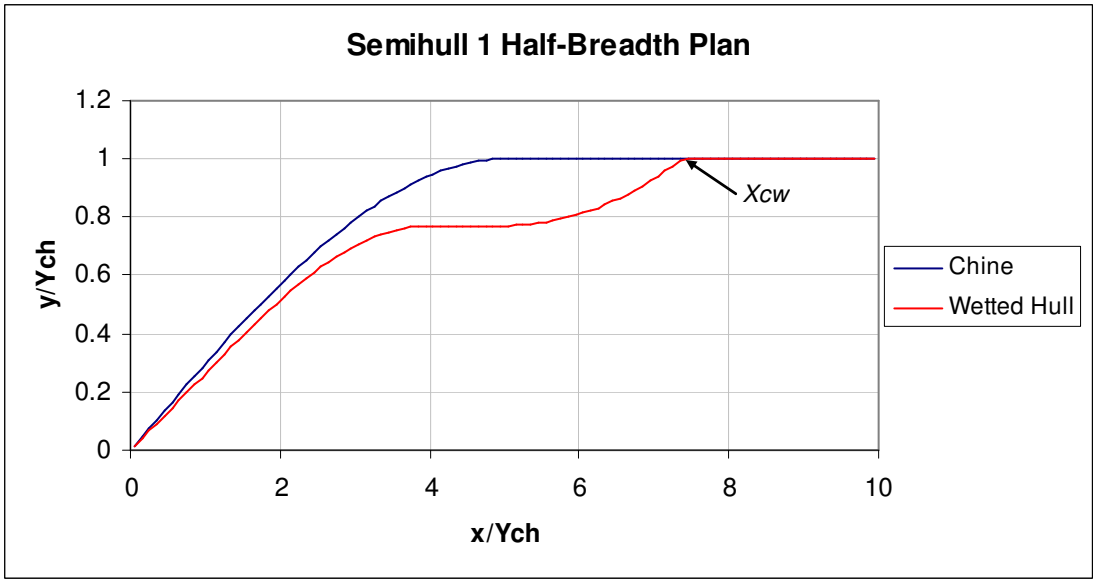

Figure 4.5 – Running half-breadth plan of Semihull 1

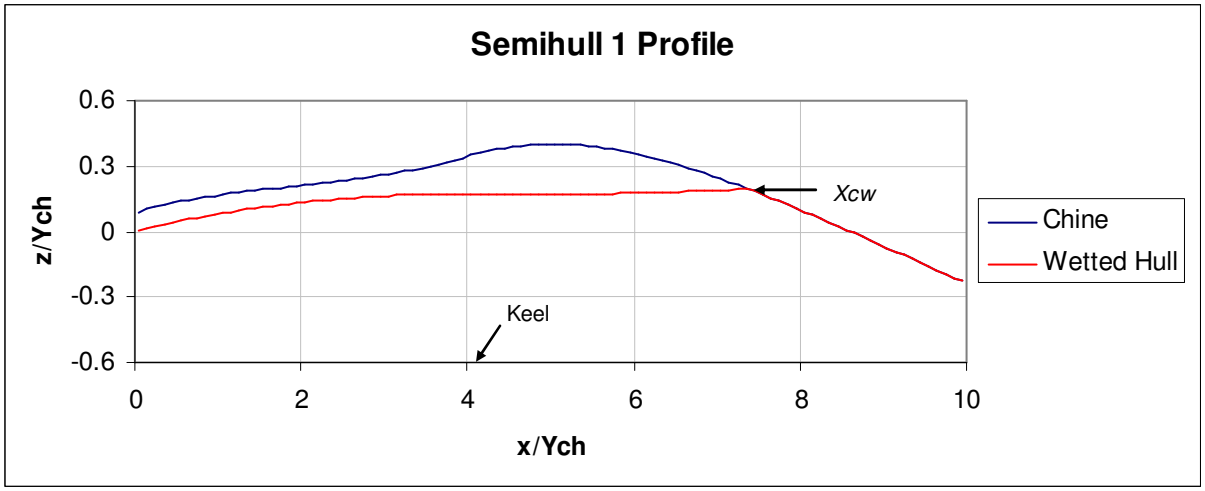

Figure 4.6 – Running Profile of Semihull 1

As can be seen in Figure 4.4, a rising jet head has been taking into account. This jet-head has been computed using an approximate method from Vorus (1996). *Xcw* indicated on Figure 4.5 and 4.6 is the chine wetting point, where the jet-head has risen up the hull sides to intersect the chine. The jet-head offset is shown on Figure 4.5 and lies under the chine intersection at *Xcw*, after which the jet-head and the chine are coincident. The implication of Figure 4.5 is that the hard chine is not involved with the hull surface flow until it wets at 75% of the length aft (for this prototype). The forebody can therefore be viewed as chineless, with the forward lines like those of a conventional fine-hulled displacement ship. Note from Figures 4.4 and 4.6 that, unlike planing craft, the trim is zero consistent with displacement vessel attitude. This allows the application of a surface (or wave) piercing stem, as shown in Figure 4.6. The subsurface stem is pointed over its wetted depth.

The rapid reduction in deadrise angle, as depicted in Figure 4.4 and plotted specifically in Figure 4.7, is responsible for the rapid rise of the jet-head toward chine wetting seen in Figure 4.5.

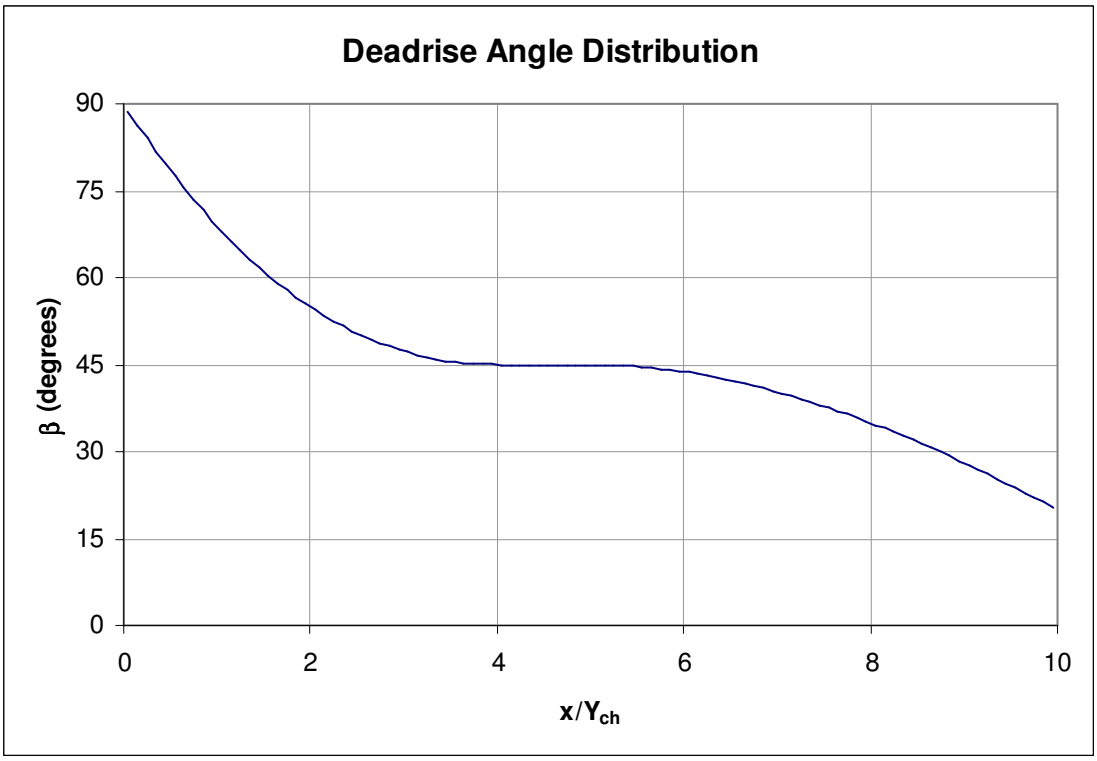

Figure 4.7 – Deadrise angle distribution in *x* of Semihull 1

4.2.1 Maruo Calculation

The high rate of deadrise reduction provides the high-lift stern. The lift coefficient distribution in *x* over the length is shown in Figure 4.8. Figure 4.8 depicts total lift, which includes the hydrostatic lift due to gravity. The total lift has been determined from the hydrostatic lift distribution and the dynamic lift distribution from the vortices of the generalized Maruo solution of Section 3.1. The centerplane source distribution, being without circulation, produces no lift. The lift and drag coefficients are defined on vessel half-beam (as in equations 3.45 and 3.47) rather than length. The drag components of the Maruo analysis are spray drag, induced drag, and wave drag due to waterplane wave making vortices.

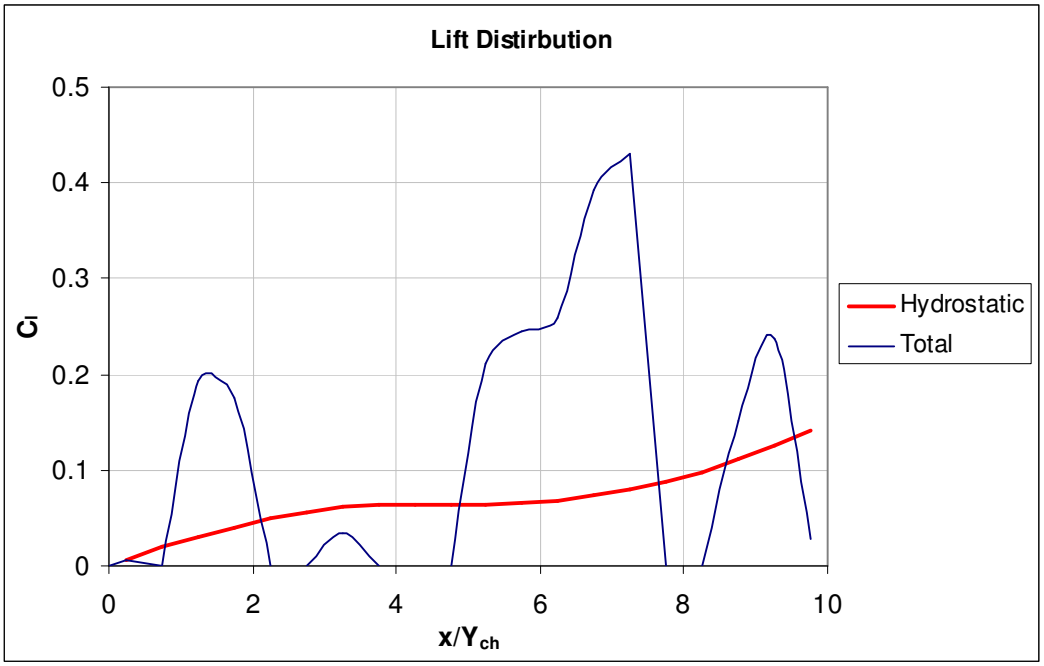

Figure 4.8 – Lift distribution of Semihull 1 at *Fn* = 1.06

It is noted that the general Maruo solution for the Semihull 1 produces negative lift between x/Y_{ch} equals 2 and 5. The negative lift is not physically acceptable; however, it is well known that ventilation in this area does occur for high speed hull forms with buttock lines of high slope at the bow. For the purposes of this analysis, the dynamic pressure was superimposed with the hydrostatic pressure. Any resulting negative pressure was zeroed (as shown in Figure 4.8) when computing the total lift. Proper investigation of this problem would require a ventilation analysis; however, a ventilation analysis is not of interest here and is beyond the scope of this work.

It can also be seen, from Figure 4.8, that the maximum lift is produced at the chine wetting point with a majority of the lift being produced just forward of that. This signifies the importance of the deadrise angle distribution in this area.

Figure 4.9 – Projected waterplane discretization for Maruo analysis

Figure 4.9 depicts the discretization of vortices of the waterplane for the Maruo analysis. Each transverse line is divided into twenty equally spaced line vortices.

4.2.2 Michell-Ogilvie Calculation

The source wave resistance was calculated by the high speed Michell formulation of Section 2.3. The centerplane discretization is shown in Figure 4.10, including the wake extension calculated by Vorus' (March 2009) wake trench formulation. The hull model is composed of 20 panels in 0 to *L*, and 20 panels over the draft. The wake trench model is composed of 15 panels over the length and 20 panels over the depth for *Fn* of 1.06.

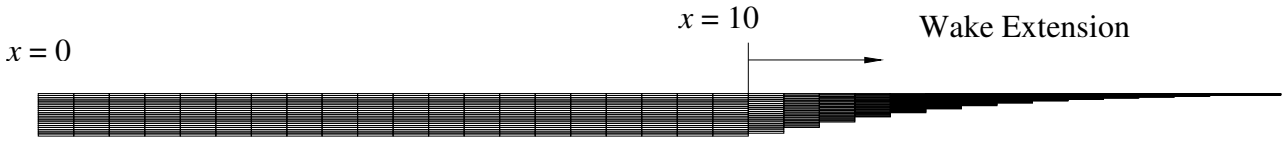

Figure 4.10 – Panel model for high speed Michell calculation of Semihull 1 at *Fn* = 1.06

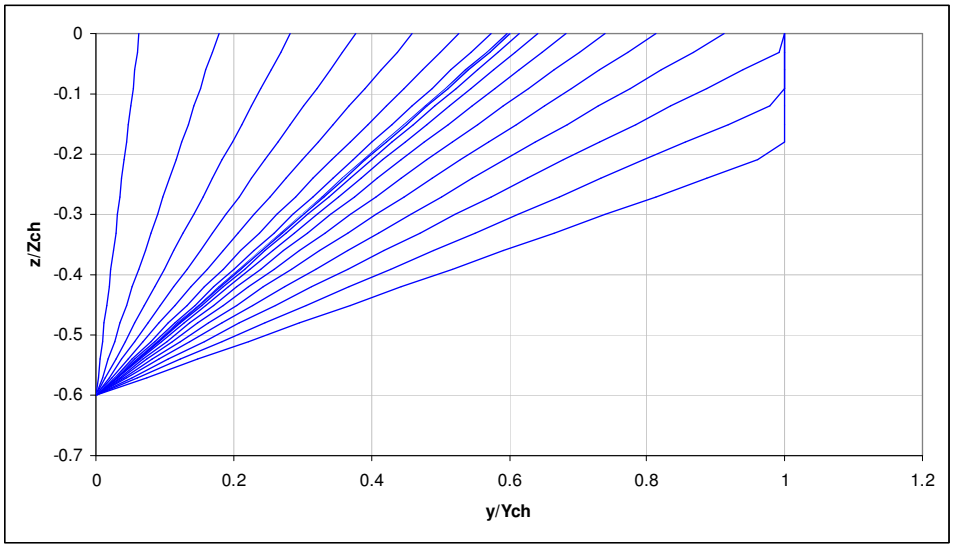

Figure 4.11 – Body plan for centerplane panelization

The body plan for computing $q(x,z)$ is shown in Figure 4.11. Note the difference between Figure 4.11 and the wetted body plan, Figure 4.4. The Michell's integral calculation is with respect to the undisturbed water surface. Therefore, the jet rise present in Figure 4.4 has been truncated on Figure 4.11. This is a discretization error from dividing the offset into 20 equal elements at each x.

Figure 4.12 is a plot of Michell wave resistance over a range of Froude numbers that include the design Froude number of 1.060.

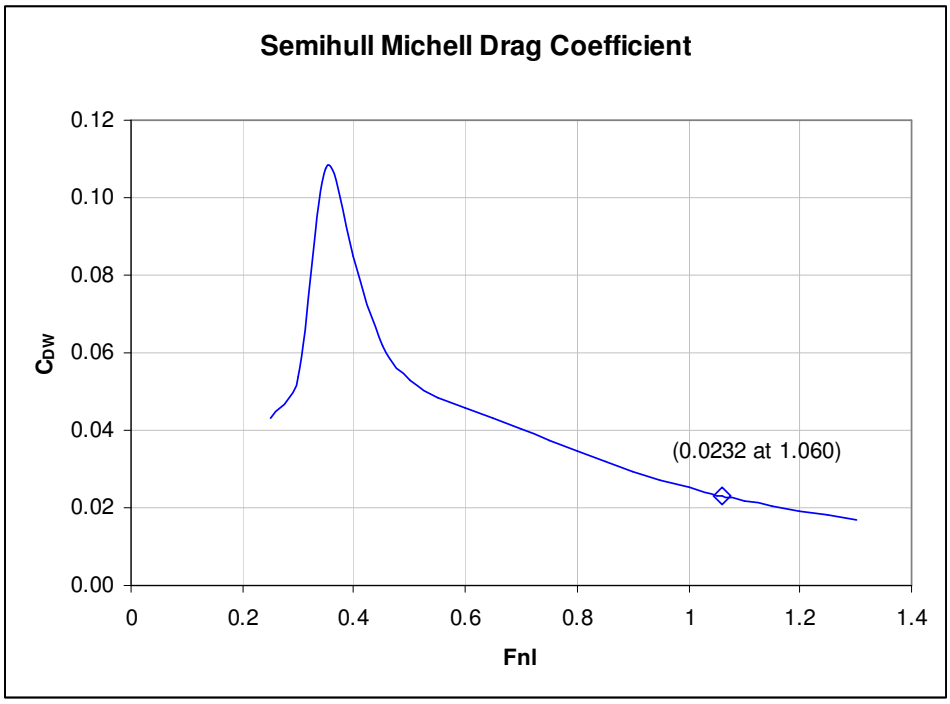

Figure 4.12 – Michell-Ogilvie's Wave Resistance versus Froude number

The non-dimensionalization of Figure 4.12 is the same as on Figure 4.8 in terms of half-breadth.

4.2.3 Hybrid Solution

The solution for lift and drag due to the odd and even flow are additive by linearity (Section 1.2). However, there remains two additional components of drag that have yet to be discussed. First, the transom hydrostatic drag is due to the axially unbalanced hydrostatic pressure from the wake defect associated with separation of flow along the transom base. Second, the viscous drag is from the ITTC friction line and is the only empiricism present in the analysis. Both of these components have been non-dimensionalized in terms of half-beam.

Table 4.3 summarizes the predicted prototype design performance after the superposition of the hydrodynamic components.

Table 4.3 – Analysis Summary – Prototype hybrid Semihull 1 calm water performance

Hull length/Ych		10	
Vessel operating draft/Ych		0.6	
Vessel operating trim	τ	0.0	deg.
Vessel speed	*U*	50.0	knots
Design Beam Froude No.	*Fnb*	3.353	
Design Length Froude No.	*Fnl*	1.060	
Reynold's No.	*Re*	1.40E+09	
Hydrostatic lift		0.6841	
Dynamic lift		0.4992	
Total Lift	C_L	1.1833	
Viscous drag		0.0693	
Transom drag		0.0433	
Drag due to waterplane vortices (wave, spray, induced)		0.1304	
Wave drag due to centerplane wave-making sources		0.0232	
Total Drag	C_D	0.2662	
Lift/Drag Ratio	*L/D*	4.45	

4.2.3 Comparison of Semihull to Displacement Hull

At this point it is useful to explore the question of whether the hybrid semihull form, which develops dynamic lift but also a dynamic lift related component of wave resistance has the potential to compete with the non-lifting displacement hull, which develops only the one displacement component of wave resistance.

For this analysis the parabolic hull form 1846B of Appendix B was compared to the Semihull 1 of the previous sections. The parabolic hull form was set with the same speed, length, and beam of the semihull. However, in order to achieve the same weight, a draft adjustment from $T/L = 0.060$ to $T/L = 0.072$ was required. The trim was set to zero, giving an $Xcg/L = 0.5$ with the fore-and-aft symmetry.

The calculated wave resistances of both the parabolic hull form and the hybrid semihull from the centerplane sources via the Michell-Ogilvie solution of Chapter 2 are shown in Figure 4.13. The resistance for the Semihull is just the displacement wave resistance from Figure 4.12.

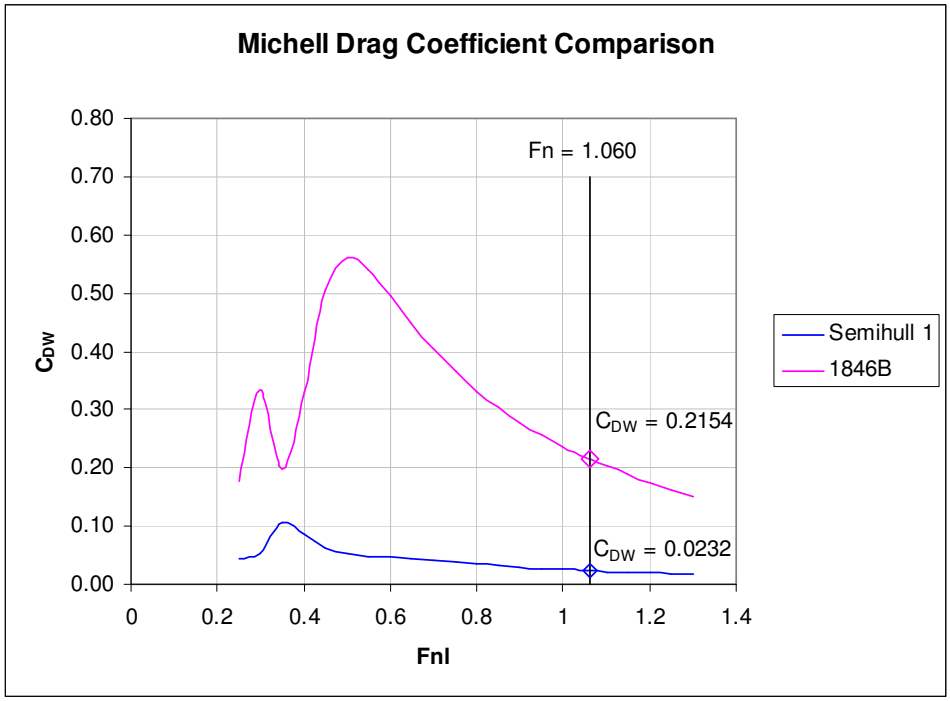

Figure 4.13 – Comparison of Michell-Ogilvie Wave Resistance for Semihull 1 and parabolic hull form

A summary of the results for the comparison of the semihull and parabolic hull from at *Fn* = 1.060 (50 knots) can be found in Table 4.4.

Table 4.4 – Hydrodynamic comparison of hybrid Semihull 1 to parabolic hull form 1846B

	Semihull 1	1846B
Hydrostatic lift	0.6841	1.1833
Dynamic lift	0.4992	0.0000
Total Lift	1.1833	1.1833
Viscous drag	0.0693	0.0509
Transom drag	0.0433	0.0000
Drag due to waterplane vortices (wave, spray, induced)	0.1304	0.0000
Wave drag due to centerplane wave-making sources	0.0232	0.2154
Total Drag	0.2662	0.2663
Lift/Drag Ratio	4.45	4.44

While the comparison of Table 4.4 yields very similar results for calm water performance when comparing the Semihull to the displacement hull form, it is well known that displacement monohulls of these proportions cannot be run at Froude number greater than about 0.35 because of the prohibitively large wave resistance developing beyond that point, as demonstrated in Figure 4.13.

Since displacement wave resistance (from centerplane sources) is proportional to beam squared, the direction taken by the naval architecture field striving for faster and faster ships is to design them to be thinner and thinner. But as the monohull becomes thinner and thinner it loses waterplane inertia, as beam cubed, and may encounter transverse instability. To counter the transverse instability the monohulls are expanded to multihulls (e.g. catamarans and trimarans). But with the hull surface area varying most strongly with length and draft, and not beam, the viscous resistance tends to increase roughly proportional to the number of multihulls.

It can be argued based on the analysis presented here that this approach of resorting to multihulls may not have the potential to lead to optimum designs, at least not from the standpoint

of calm-water resistance. The semi-displacement/semi-planing concept (i.e. the Semihull) is suggested as a competing approach to very thin multihulls.

4.3 Semihull Variations

In an effort to optimize the Semihull, various parameters from Table 4.2 were adjusted to develop a more efficient design. For the purposes of this work the, the deadrise angle parameters were varied while the principal dimensions remained constant. Table 4.5 provides a summary of the key dimensions of the semihull variations. Semihull 1 is the base case studied in Section 4.2. The deadrise angle parameters were changed one at a time for Semihulls 2 to 4. The modifications (as compared to Semihull 1) are highlighted in yellow. Semihull 5 is a compilation of all modifications made to Semihulls 2 to 4.

Table 4.5 – Geometric Parameters for Semihull Variation

		Semihull 1	Semihull 2	Semihull 3	Semihull 4	Semihull 5
Length of waterline	L	10	10	10	10	10
Chine offset at transom	Y_{ch}	1	1	1	1	1
Vessel operating draft	H_T	0.6	0.6	0.6	0.6	0.6
Slope of chine offset at entry	Y_{0x}	0.3	0.3	0.3	0.3	0.3
Forward chine tangent point, forward from transom	L_{ac}	5	5	5	5	5
Deadrise angle at entry	β_0	90	90	90	90	90
Rate of change of deadrise angle at entry	β_{0x}	-25	-35	-25	-25	-35
Intermediate constant value of deadrise angle	β_{01}	45	45	45	50	50
Deadrise angle at transom	β_1	20	20	20	20	20
Rate of change of deadrise angle at transom	β_{1x}	-8.5	-8.5	-10	-8.5	-10
Forward deadrise tangent point, forward from transom	L_{ab}	6	6	6	6	6
Aft deadrise tangent point, forward from transom	L_{bb}	5	5	5	5	5

The various deadrise angle distributions are shown in Figure 4.14. The distribution for Semihull 1 is not easily seen because it is overlapped by another Semihull's distribution at all longitudinal positions.

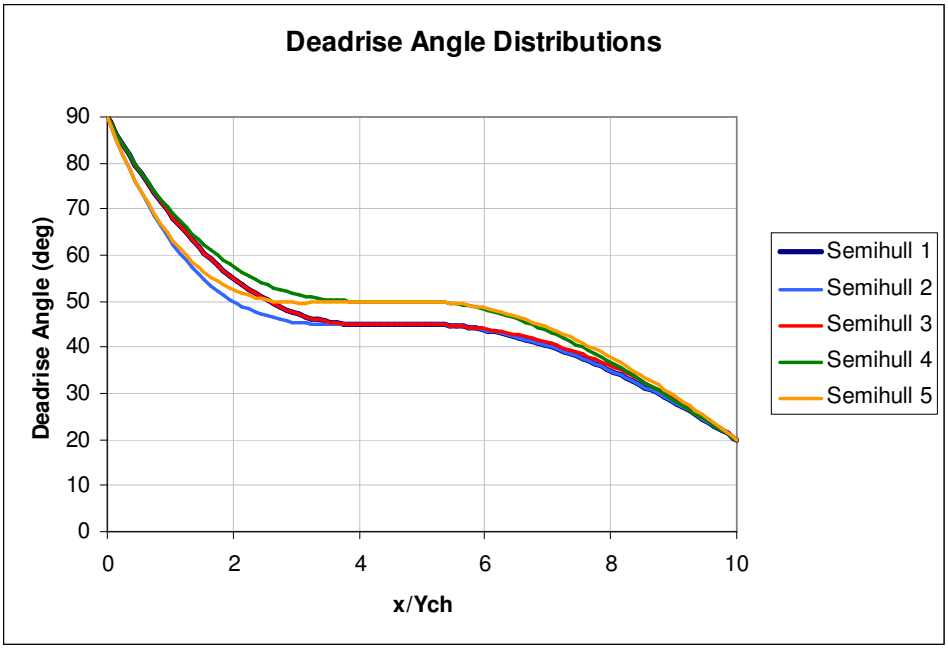

Figure 4.14 – Deadrise Angle Distributions for Semihull Variations

Table 4.6 – Calm Water Performance of Semihull Variations at *Fn* = 1.06

		Semihull 1	Semihull 2	Semihull 3	Semihull 4	Semihull 5
Hydrostatic lift		0.6841	0.7053	0.6737	0.6245	0.6348
Dynamic lift		0.4992	0.5127	0.5760	0.7515	0.7468
Total Lift	C_L	1.1833	1.2180	1.2496	1.3760	1.3816
Viscous drag		0.0693	0.0669	0.0696	0.0735	0.0711
Transom drag		0.0433	0.0433	0.0433	0.0433	0.0433
Drag due to waterplane vortices (wave, spray, induced)		0.1304	0.1100	0.1282	0.1654	0.1557
Wave drag due to centerplane wave-making sources		0.0232	0.0250	0.0226	0.0248	0.0263
Total Drag	C_D	0.2662	0.2452	0.2637	0.3069	0.2964
Lift/Drag Ratio	*L/D*	4.45	4.97	4.74	4.48	4.66

The results of the hybrid analysis for the five variations of the Semihull can be found in Table 4.6. The maximum lift in each category has been highlighted in orange, while the minimum drag value for each category has been highlighted in blue for Semihulls 2 to 5. The transoms on all of the Semihull variations are identical in geometry; therefore, they offer the same amount of drag.

Here we can see that by decreasing the rate of change of deadrise angle at entry (β_{0x}) in Semihull 2, we decrease the total drag while the total lift slightly increases when compared to

that of Semihull 1. The main contributor to the higher efficiency of Semihull 2 is the decreased drag due to the waterplane vortices. The lower vortex strength offers lower drag and lower dynamic lift. However, by decreasing the rate of change of deadrise angle at entry from -25 to -35, the bow of Semihull 2 becomes fuller when compared to that of Semihull 1. This offers an increase in hydrostatic and dynamic lift. The fuller hull in the bow of Semihull 2 does not significantly increase the wave drag due to the centerplane sources at the speed analyzed.

Decreasing the rate of change of deadrise angle at the transom (β_{1x}), as in Semihull 3, offers an increase in dynamic lift while sacrificing minimal hydrostatic lift. This is due to the fact that the slope of the buttock lines at the transom are increasing (in the negative sense) providing increasing dynamic lift. This agrees with the description of the Semihull in which the aft hull lines are designed to be similar to those of a planing hull, thus, generating a majority of the dynamic lift. Care with this hull modification must be taken so that the drag due to the wave making vortices does not increase significantly.

The third modification made to the base case was to increase the intermediate constant value of deadrise angle (β_{01}) from 45 degrees to 50 degrees. This hull modification in Semihull 4 significantly increased the dynamic lift. While this modification also decreased the hydrostatic lift, the total lift increased significantly when compared to Semihull 1. While this hull modification offered a significant increase in lift, it also offered a significant increase in drag. All aspects of drag (accept transom) increased. This resulted in a lift-to-drag ratio very similar to that of Semihull 1.

Semihull 5 is a compilation of all of hull modifications made thus far. While all of the changes seemed to be the most favorable for lift, an increase in drag was also obtained. While

Semihull 5 may have better calm water performance values when compared to Semihull 1, it is not the best designed when compared to all five hulls.

Of all of the modifications made to Semihull 1, adjusting the rate of change of deadrise angle at entry seemed to have the most favorable impact, as seen in Semihull 2. While this hull form may not offer the most lift, it does offer the least drag and the best lift-to-drag ratio of the hulls compared here.

5.0 Conclusion

In this work, a hybrid method was presented for computing lift and drag of semi-planing/ semi-displacement slender hull forms. This was done by separating the linear problem into odd and even parts, solving each part independently, and then superimposing the solutions. The odd part was solved using a high-speed form of Michell's integral (1898) for thin ships, and the even part was solved by using a general form of Maruo's (1965) flat ship theory.

Michell's integral (1898) has been used for many years. However, it has proved to produce unacceptable results at high speeds. A method was introduced here utilizing Ogilvie's (1972) equation for bow wave flow. Vorus and Taravella (2008) developed a general solution to Ogilvie's (1972) equation which provided a near field solution. This near field solution was then collapsed to the centerplane to obtain the centerplane source distribution for direct use in Michell's integral (1898). As can be seen in this work, the results of the general high-speed Michell's integral compared quite nicely to model test results.

High-speed vessels with transom sterns also produce a wake trench. Vorus (2009) developed a solution for determining the length of the wake trench. This was utilized in the present theory.

Maruo (1967) presented an equation for low-aspect ratio planing with gravity. In his work, the boundary condition is satisfied on the waterplane of general flat-type vessels following the infinite Froude number work of Von Karman' (1929) and Wagner (1932). Maruo's solution was limited to waterplanes of simple geometric shapes (i.e. delta). Maruo admitted that this equation was difficult to solve because of the singular nature of the problem. Vorus and Taravella (2009) developed a general closed form solution to Maruo's equation. The results are presented here and compare quite well to the results of Maruo (1967) and Tuck (1975). While

some future development may still be necessary, the results of the general Maruo equation are adequate for use in the hybrid theory presented here.

The presentation of the hybrid method led to the development of the Semihull concept—a vessel which has properties of both a thin displacement hull and a high-speed planing hull.

Optimization proves that an increase in displacement will increase the hydrostatic lift while only slightly increasing the wave making resistance due to displacement flow. Therefore, a good balance is needed between hydrostatic and dynamic lift. The results also indicate that much of the dynamic lift is developed near the stern. This gives indication that the Semihull obtains additional lift from the wave generated by its form. The center of this lift changes with speed variation, thus resulting in a change in trim of the Semihull, unlike displacement vessels. The Semihull is also shown to be a viable alternative to multi-hulled high speed vessels.

As seen from the results of this work, the hybrid method provides a feasible method for predicting calm water performance of semi-planing/semi-displacement hull forms utilizing the classical methods of Michell (1898), Ogilvie (1972) and Maruo (1965). While additional testing and numerical verification may be necessary, this method seems to compare quite well to the available data.

References

1. Abramowitz, M., and Stegun, I.A., *Handbook of Mathematical Functions,* Dover Publications, 1964.

2. Cole, Susan, "A Simple Example from Flat-Ship Theory", *Journal of Fluid Mechanics*, Vol. 189, 1988.

3. Doctors, L.J. and Beck, R.F., "The Separation of Flow Past a Transom Stern," *Proc of the 1st International Conference on Marine Research and Transportation (ICMRT '05)*, Ischia, Italy, September 2005.

4. Faltinsen, Odd and Sun, Hui, "The Influence of Gravity on the performance of Planing Vessels in Calm Water," *Journal of Engineering Mathematics,* Vol. 58, August 2007.

5. Gradshteyn, I.S., Ryzhik, I.M., *Table of Integrals, Series, and Products,* Sixth Edition, Academic Press, 2000.

6. Hildebrand, F. B., *Advanced Calculus for Application,* Second Edition, Prentice Hall, 1976.

7. Lamb, G. R., "High-Speed, Small Naval Vessel Technology Development Plan," Carderock Division Naval Surface Warfare Center, NSWCCD-20-TR-2003/09, May 2003

8. Maruo, H., "High and Low-Aspect Ratio Approximation of Planing Surfaces," *Schiffstechnik,* 1967.

9. *Mathematica Online Integrator,* integrals.wolfram.com, Wolfram Research, Inc., 2008.

10. Michell, J., "The Wave Resistance of a Ship," *Philosophical Magazine,* 1897.

11. Newman, J. N., *Marine Hydrodynamics,* The MIT Press, 1977.

12. Ogilvie, T. F., *NA 525, Naval Hydrodynamics I, Lecture Notes,* University of Michigan, Ann Arbor, Michigan, Fall 1969.

13. Ogilvie, T. F., "The Waves Generated by a Fine Ship Bow," *Ninth Symposium on Naval Hydrodynamics,* Paris, August 1972.

14. Savitsky, D., "Hydrodynamic Design of Planing Hulls," *Marine Technology,* SNAME Vol. 1, 1964.

15. Troesch, Armin W., "On the Hydrodynamics of Vertically Oscillating Planing Hulls," *Journal of Ship Research,* Vol. 36, 1992.

16. Tuck, E. O., "Low-Aspect-Ratio Flat-Ship Theory", *Journal of Hydronautics,* Vol. 9, No. 1, January 1975.

17. Tuck, E. O., "A Comparison of Linear and Nonlinear Computations of Waves Made by Slender Submerged Bodies," *Journal of Engineering Mathematics,* 42 (2002) 255-264.

18. Tuck, E. O., Scullen, D. C., and Lazauskas, L., "Ship-Wave Patterns in the Spirit of Michell", *Proceeding of the IUTAM Symposium of Free-Surface Flows,* July 2000.

19. Tuck, E. O., Scullen, D. C., and Lazauskas, L., "Wave Patterns and Minimum Wave Resistance for High-Speed Vessels," *24th Symposium on Naval Hydrodynamics*, Fukuoka, Japan, July 2002.

20. Von Karman', T., "The impact of seaplane floats during landing," NACA TN 321, Washington D.C., October 1929.

21. Vorus, William S., "A Flat Cylinder Theory for Vessel Impact and Steady Planing Resistance," *Journal of Ship Research,* Volume 40, Number 2, June 1996.

22. Vorus, William S., "The Importance of Wave-Making in the Lift and Resistance of Planing Craft," submitted to the *Journal of Ship Research,* April 2005.

23. Vorus, William S., "Tools for Semi-Planing/Semi-Displacement Ship Design with Applications," NEMO Report on Year 1, June 20, 2005.

24. Vorus, William S., "Closure of the Deep Wake Trench of High Speed Ships," *Journal of Ship Research,* Volume 53, Number 1, March 2009.

25. Vorus, William S. and Taravella, Brandon M., "Reformulation of Maruo Theory for General Cases - #10", personal manuscript, February 2009.

26. Vorus, William S. and Taravella, Brandon M., "A Generalized Michell's Integral for the Wave Resistance of Slender High-Speed Ships", personal manuscript, November 2008.

27. Wagner, H., "Uber stoss-und gleitvorgange an der oberflache von flussigkeiten," *Zeitschrift fur Angewandte Mathematik und Mechanik,* Volume 12, August 1932.

28. Xie, N., Vassaloz, D. and Jasionowski, A., "A Study of Three-Dimensional Planing Surface", *Ocean Engineering,* Volume 32, 2005.

Appendix A – Ogilvie Integral

From equation (36)

$$I = \int_{s=0}^{\infty} e^{\zeta s^2} \cos\left(ys^2\right)\sin\left(\sqrt{\kappa}(x-\xi)s\right)ds \tag{A1}$$

Substitute $K = \sqrt{\kappa}(x-\xi)$ and use Euler's formula.

$$I = \int_{s=0}^{\infty} e^{\zeta s^2}\left[\frac{e^{iys^2}+e^{-iys^2}}{2}\right]\left[\frac{e^{iKs}-e^{-iKs}}{2i}\right]ds \tag{A2}$$

$$I = \frac{1}{4i}\int_{s=0}^{\infty}\left[e^{(\zeta+iy)s^2+iKs} - e^{(\zeta+iy)s^2-iKs} + e^{(\zeta-iy)s^2+iKs} - e^{(\zeta-iy)s^2-iKs}\right]ds \tag{A3}$$

$$I = \frac{1}{4i}\left[I_1 - I_2 + I_3 - I_4\right] \tag{A4}$$

Solve integrals using equation 3.322.2 of Gradshteyn and Ryzhik (2000).

$$I_n = \int_0^{\infty}\exp\left(-\frac{x^2}{4\beta_n} - \gamma_n x\right)dx = \sqrt{\pi\beta_n}\,\exp\left(\beta_n\gamma_n^2\right)\left[1-\Phi\left(\gamma_n\sqrt{\beta_n}\right)\right] \tag{A5}$$

Where Φ is the error function.

For I_1, $\beta_1 = -\dfrac{1}{4(\zeta+iy)}$ and $\gamma_1 = -iK$

For I_2, $\beta_2 = -\dfrac{1}{4(\zeta+iy)}$ and $\gamma_2 = iK$

For I_3, $\beta_3 = -\dfrac{1}{4(\zeta-iy)}$ and $\gamma_3 = -iK$

For I_4, $\beta_4 = -\dfrac{1}{4(\zeta-iy)}$ and $\gamma_4 = iK$

It is now necessary to take the derivative with respect to *y*.

$$\frac{dI}{dy} = \frac{1}{4i}\left[\frac{dI_1}{dy} - \frac{dI_2}{dy} + \frac{dI_3}{dy} - \frac{dI_4}{dy}\right] \tag{A6}$$

Taking the derivative of the error function as $\frac{d}{dz}\Phi(Z) = \frac{2}{\sqrt{\pi}}e^{-Z^2}$

$$\frac{dI_n}{dy} = \frac{1}{2}\sqrt{\frac{\pi}{\beta_n}}\exp\left(\beta_n\gamma_n{}^2\right)\left[1-\Phi\left(\gamma_n\sqrt{\beta_n}\right)\right]\frac{d\beta_n}{dy} + \gamma_n{}^2\sqrt{\pi\beta_n}\exp\left(\beta_n\gamma_n{}^2\right)\left[1-\Phi\left(\gamma_n\sqrt{\beta_n}\right)\right]\frac{d\beta_n}{dy}$$

$$-\sqrt{\pi\beta_n}\exp\left(\beta_n\gamma_n{}^2\right)\frac{2}{\sqrt{\pi}}\exp\left(-\beta_n\gamma_n{}^2\right)\frac{\gamma_n}{2\sqrt{\beta_n}}\frac{d\beta_n}{dy} \tag{A7}$$

The complex error function (also known as the Faddeeva function), denoted by *w,* (Abramowitz and Stegun, 1964) can be used such that: $w\left(i\gamma_n\sqrt{\beta_n}\right) = \exp\left(\beta_n\gamma_n{}^2\right)\left[1-\Phi\left(\gamma_n\sqrt{\beta_n}\right)\right]$

$$\frac{dI_n}{dy} = \frac{1}{2}\sqrt{\frac{\pi}{\beta_n}}w\left(i\gamma_n\sqrt{\beta_n}\right)\frac{d\beta_n}{dy} + \gamma_n{}^2\sqrt{\pi\beta_n}\,w\left(i\gamma_n\sqrt{\beta_n}\right)\frac{d\beta_n}{dy} - \gamma_n\frac{d\beta_n}{dy} \tag{A8}$$

$$\frac{dI_n}{dy} = \sqrt{\pi}\,w\left(i\gamma_n\sqrt{\beta_n}\right)\frac{d\beta_n}{dy}\left[\frac{1}{2}\sqrt{\frac{1}{\beta_n}} + \gamma_n{}^2\sqrt{\beta_n}\right] - \gamma_n\frac{d\beta_n}{dy} \tag{A9}$$

Taking the derivatives of the β_n equations above, we have:

$$\frac{d\beta_1}{dy} = \frac{d\beta_2}{dy} = \frac{i}{4}(\zeta + iy)^{-2} \tag{A10}$$

$$\frac{d\beta_3}{dy} = \frac{d\beta_4}{dy} = -\frac{i}{4}(\zeta - iy)^{-2} \tag{A11}$$

Appendix B – Ogilvie Test Models

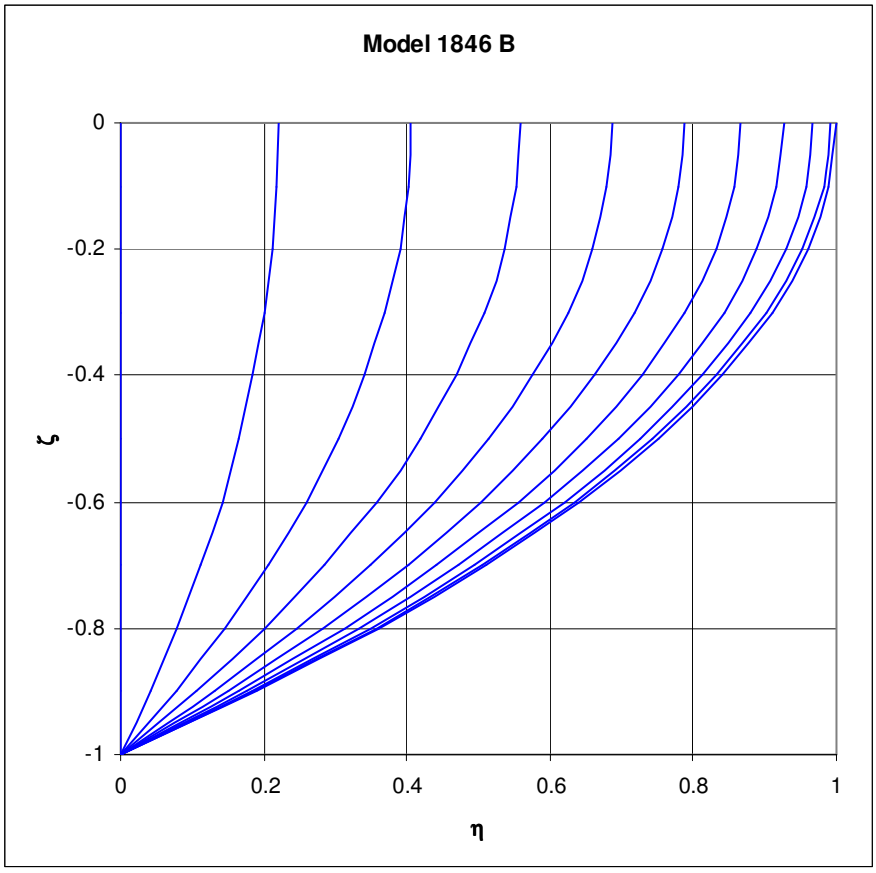

Figure B1 – Body Plan of Model 1846 B

The hull offsets are defined by:

$$\eta = \left(1-\zeta^2\right)\left(1-\xi^2\right)\left(1+0.2\xi^2\right) \tag{B1}$$

Table B1 – Model 1846 B Form Coefficients

Block Coefficient	0.462
Prismatic Coefficient	0.693
Mid-Section Coefficient	0.667
Waterplane Coefficient	0.693
½ Angle of Entrance on LWL	12.7°

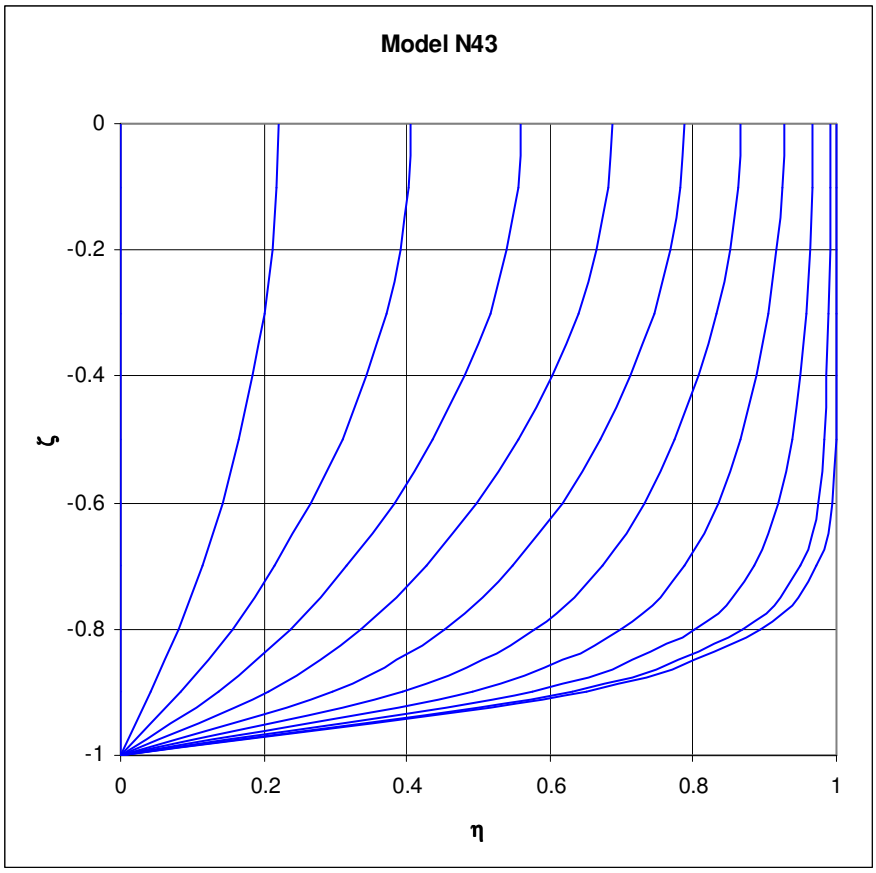

Figure B2 – Body Plan of Model N43

The hull offsets are defined by:

$$\eta = (1-\zeta^2)(1-\xi^2)(1+0.2\xi^2)+\zeta^2(1-\zeta^8)(1-\xi^2)^4 \qquad \text{(B2)}$$

Table B2 – Model 1846 B Form Coefficients

Block Coefficient	0.561
Prismatic Coefficient	0.617
Mid-Section Coefficient	0.909
Waterplane Coefficient	0.693
½ Angle of Entrance on LWL	12.7^o

Vita

Brandon Taravella was born in New Orleans, LA and graduated Valedictorian from Archbishop Shaw High School (Marrero, LA) in 1999. He received his Bachelor of Science in Naval Architecture and Marine Engineering with Departmental Honors from the University of New Orleans in 2003. He received his Master of Science in Engineering with concentration in Naval Architecture and Marine Engineering from the University of New Orleans in 2005. Brandon became a Professional Engineer in the State of Louisiana in 2006.

From 2002 to 2008, Brandon worked his way from Naval Architect Intern up to Supervisor of Naval Architecture at Northrop Grumman Ship Systems Avondale Operations (Avondale, LA). Brandon has been an adjunct instructor for the University of New Orleans' School of Naval Architecture since 2005. He has taught classes in Introduction to Naval Architecture, Introduction to Marine Design, Form Calculations and Stability, and Marine Dynamics.

He is currently employed at J. Ray McDermott Engineering – New Orleans (New Orleans, LA) as a Principal Naval Architect.